International Journal of Machine Tools & Manufacture 184 (2023) 103980

Contents lists available at ScienceDirect

International Journal of Machine Tools and Manufacture

journal homepage: www.elsevier.com/locate/ijmactool

Deformation mechanisms and fracture in tension under cyclic bending plus compression, single point and double-sided incremental sheet forming processes

Wenxuan Peng, Hengan Ou *

Department of Mechanical, Materials and Manufacturing Engineering, Faculty of Engineering, University of Nottingham, Nottingham, NG7 2RD, UK

ARTICLE INFO

Keywords:
Ductility
Fracture
Bending under tension
Finite elements
Incremental sheet forming

ABSTRACT

This study investigates the deformation and fracture mechanisms of two testing methods, tension under cyclic bending (TCB) and tension under cyclic bending plus compression (TCBC) and their relationship to single point (SPIF) and double-sided (DSIF) incremental sheet forming processes. Experimental tests were carried out by using a bespoke TCBC test rig and a DSIF machine with grade 1 pure Ti samples. The results show the elongation-to-fracture has a high relevance to the bending depth and compression, which leads to detailed investigation to the stress and strain evolutions in the local bending region using finite element (FE) method. A new Gurson-Tvergaard-Needleman (GTN) model is proposed with a modified shear damage mechanism utilising experimental fracture strain loci to calibrate the Lode angle effect under low stress triaxiality. It is found the bending and reverse-bending stages correspond to different stress states and significantly affect the fracture occurrence in TCB, TCBC and SPIF, DSIF processes. For the first time, the stress paths in the plane of stress triaxiality and Lode parameter are used to reveal the transition of deformation modes from equi-biaxial to plane strain tension in SPIF and DSIF, as compared to the plane stress tension in TCB and TCBC. Using the new GTN model, the simulation gives accurate predictions to the elongation-to-fracture in TCB and TCBC, and the fracture depth in SPIF and DSIF with an error of less than 8% in comparison to the experimental results. Although there is a distinction between the equi-biaxial and uniaxial tension deformations, the study concludes that the TCB and TCBC tests provide an insight into the formability improvement and represent intrinsic deformation mechanisms of SPIF and DSIF processes, an ongoing research question, which has drawn considerable attention in recent years.

1. Introduction

Incremental sheet forming (ISF) is a flexible sheet metal forming process with considerable progress having been made in fundamental studies in recent years [1–5]. In the past decade, progress has also been made in using ISF based technologies for direct industrial applications [6,7]. The ISF process only requires the use of a Computer Numerical Control (CNC) milling machine or a robotic system to control a hemispherical tool moving along a pre-defined toolpath to form a blank sheet clamped at periphery. Through continuous localised deformation by the ISF tool, the blank sheet is incrementally deformed to the desired shape. Many variants such as Two-Point Incremental Forming (TPIF) and Double-Sided Incremental Forming (DSIF) have been developed in recent years in order to address a few underlying issues and further improve the formability. As shown in Fig. 1, the classification of the variants of ISF processes may be based on the method to apply supporting forces. TPIF uses an extra full or a partial die on the other side of the blank sheet to enhance forming stability (Fig. 1b). The DSIF process replaces the full or partial die with a flexible supporting tool following a specified trajectory in order to provide a localised support (Fig. 1c). Both the TPIF and DSIF processes improve the formability and accuracy in comparison to the conventional ISF process using a single tool, often called Single Point Incremental Forming (SPIF). In particular, the DSIF process keeps die-less feature and flexibility that attracts increasing research interests [8,9] with progress made towards practical implementation in automotive industry [10].

However, the underlying factors that influence the formability improvement of DSIF over SPIF processes are not fully understood. In previous experimental observations of the SPIF process, increasing a single parameter can cause a contrary impact on formability, such as tool diameter [12,13], thickness [13,14] and step size [15]. An

* Corresponding author.
E-mail address: h.ou@nottingham.ac.uk (H. Ou).

https://doi.org/10.1016/j.ijmachtools.2022.103980
Received 2 June 2022; Received in revised form 13 November 2022; Accepted 15 November 2022
Available online 22 November 2022

Nomenclature

A, B, n	Johnson-Cook's constitutive model parameters
D_s, $\dot{D}_s$	Shear damage variable and its rate
E	Young's modulus
F_N	Total volume fraction can be nucleated
f	Void volume fraction
f^*	Effective void volume fraction
f_c	Critical void volume fraction
f_f	Final void volume fraction
f_{growth}	Void volume fraction of hydrostatic stress
$f_{nuleation}$	Void volume fraction of void nucleation
f_{shear}	Void volume fraction of shear damage
g_0	Lode dependency function
$\boldsymbol{I}$	Second order identity tensor
J_3	Third stress invariant
k	Weight factor of stress triaxiality over Lode angle effect
k_w	Shear damage rate parameter
n_s	Power constant for shear damage evolution
q_1 , q_2, q_3	GTN model constants
q_4	Void volume fraction exponent for idealised cell structure
$\boldsymbol{S}$	Deviatoric stress tensor
S_N	Standard deviation for void nucleation
ε_f^s	Plastic strain for shear fracture
ε_N	Mean value of the normal distribution of nucleation strain
$\boldsymbol{d\varepsilon^p}$	Plastic strain rate tensor
$\dot{\varepsilon}_{kk}^p$	Trace of the plastic strain rate tensor
$\overline{\varepsilon}_M^p$, $\dot{\overline{\varepsilon}}_M^p$	Equivalent plastic strain and its rate
η	Stress triaxiality
$\eta_{lim}^{(+)}$, $\eta_{lim}^{(-)}$	Positive and negative cut-off values of stress triaxiality
θ_L	Lode angle
ν	Poisson's ratio
ξ	Lode angle parameter
$\boldsymbol{\sigma}$	Stress tensor
$tr(\boldsymbol{\sigma})$	Trace of stress tensor
σ_{eq}	Equivalent von Mises stress
σ_{kk}	Hydrostatic stress
σ_m	Mean stress
σ_Y	Yield stress of the undamaged material

appreciable number of studies focus on the local deformation around the tool contact point and indicate the significance of plane strain stretching, bending-under-tension and through-thickness shear as the reasons for achieving large strain under SPIF processing condition [16,17]. Based on the studies utilising finite element (FE) simulation [18] and analytical models for stress analysis [9,19,20], the deformation mechanisms of SPIF and DSIF are considered to be localised bending under tension combined with through-thickness shear and compression. FE simulation helps to provide an in-depth evaluation of fracture mechanisms in SPIF with the use of damage models, such as Gurson-Tvergaard-Needleman (GTN) [21,22] and Lemaitre continuum damage models (CDM) [3]. Although accurate damage predictions were reported in modelling the SPIF process [23–25], distinctions remain between the deformation mechanisms and formation of fracture in SPIF and DSIF processes. The specific role of the additional compression by the support tool in the DSIF to the formability improvement is still an outstanding question.

In view of experimental validation, localised contact and deformation in a small region makes the conventional testing and measurement methods inadequate to capture the deformation and fracture behaviour in both SPIF and DSIF processes. Emmens and Boogaard [26] proposed a Tension under Cyclic Bending (TCB) as a simplified representation of the deformation mode in the SPIF process. Under the TCB test condition, the samples can achieve a much larger elongation-to-fracture than those obtained from the common tensile test for both steel and aluminium sheet materials. To investigate the DSIF process, Ai et al. [19] developed a Tension under Cyclic Bending and Compression (TCBC) test, in which additional compression is applied to obtain superior elongation and formability over uniaxial tensile, TCB and Tension under Continuous Compression (TCC) tests.

Fig. 2 shows the schematics of the TCB, TCBC and their counterparts of the SPIF and DSIF. In the TCB test, 3 rollers are used to create a local bending region when the specimen is under uniaxial tensile test (Fig. 2a). The TCBC test uses an additional roller with constant compression force applied to generate a compressive zone in the bending region (Fig. 2b). The TCB test simplifies the complicated hemispherical contact problem (Fig. 2c and d) to a solely uniaxial bending under tension problem (Fig. 2a and b). The TCB and TCBC tests present similar deformation characteristics of incremental elongation by tool contact and the formability improvement by additional compression as in the SPIF and DSIF processes. The use of the standard tensile test samples and the experimental setup allow quantitative control of process parameters, such as bending radius and strain rate, and the measurement to the forming forces and local strain development.

Previous studies of TCB produced inspiring results in bending under tension mechanics [27,28], continuous ductility and hardening [29], microstructure evolution [29] and material modelling [29,30]. Results show that bending depth and cyclic tool motion speed play a key role in the process formability, resembling the effect made by the tool radius and step size in the SPIF process. Benedyk et al. [31] studied and compared in-plane strains in TCB and uniaxial tensile tests and indicated that the TCB process prolongs the stability of plastic deformation before the occurrence of necking and homogenises the strain distribution in the tensile direction. The uniformly scattered damage was assumed to enhance the necking limit which was considered as a reason for the improved formability in TCB and ISF [32]. Ai et al. [19] tested

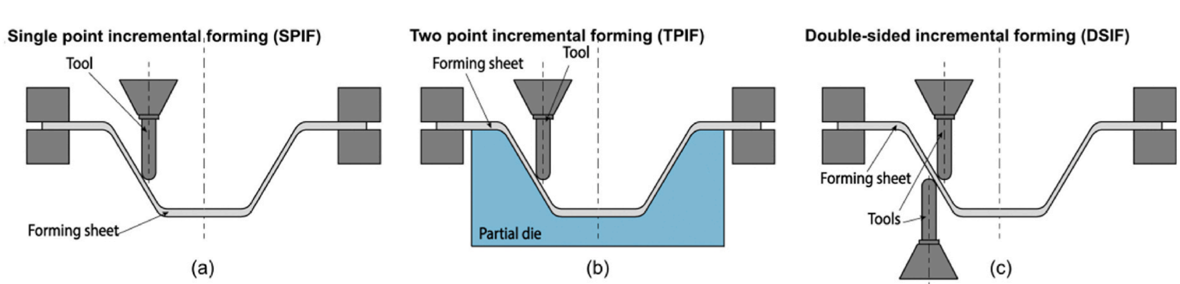

Fig. 1. Schematics of incremental sheet forming variants. (a) Single point incremental forming (SPIF), (b) Two-point incremental forming (TPIF), and (c) Double-sided incremental forming (DSIF) [11].

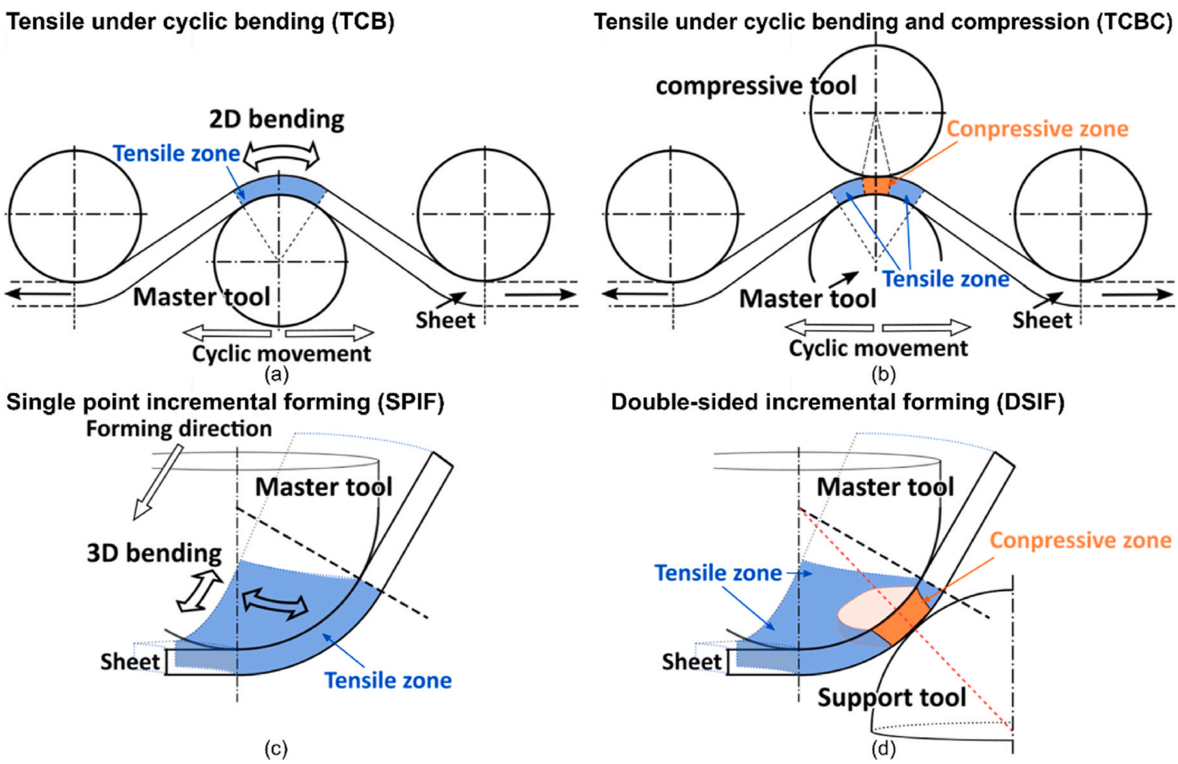

Fig. 2. Schematics of the incremental sheet forming processes and the proposed mechanical validation methods. (a) Tension under cyclic bending (TCB), (b) Tension under cyclic bending and compression (TCBC), (c) Single point incremental forming (SPIF), and (b) Double-sided incremental forming (DSIF).

AA5251-H22 and AA6082-T6 alloys with various set-up of bending, tool speed, tensile speed, compression forces and material thickness in TCB and TCBC processes. The compression force was showed as the most influential factor that was effective to enhance the formability by the bending effect. Following this result, material-based optimisation for DSIF was recommended to maximise formability. It is clear from the similarities of deformation characteristics shown in studies, more in-depth understanding of the deformation and fracture mechanisms in TCB and TCBC would help develop enhanced knowledge and expand the established capabilities of SPIF and DSIF closer to specific industrial applications.

In this study, the key factors in the formability enhancement were discovered in the TCB and TCBC tests using grade 1 pure Ti sheets. A new GTN model was developed to give an insight to the deformation characteristics and validated through uniaxial tension, TCB and TCBC tests. Accurate fracture predictions were obtained as compared to the SPIF and DSIF test results and predictions using the new GTN model. The deformation stages and the concomitant damage evolutions were analysed and explained by the stress paths as a function of stress triaxiality and Lode angle parameter, which was implemented to show the change of the local stress states, for the first time. This study presents a deeper understanding to the mechanisms of formability improvement and a valid model to evaluate the damage when bending-under-tension and compression coexist. The similarities and differences between the deformation and fracture mechanisms of the TCB and TCBC, and the SPIF and DSIF processes were identified, which provide a solid basis to use TCB and TCBC as a simple but effective means for SPIF and DSIF testing, process design and validation.

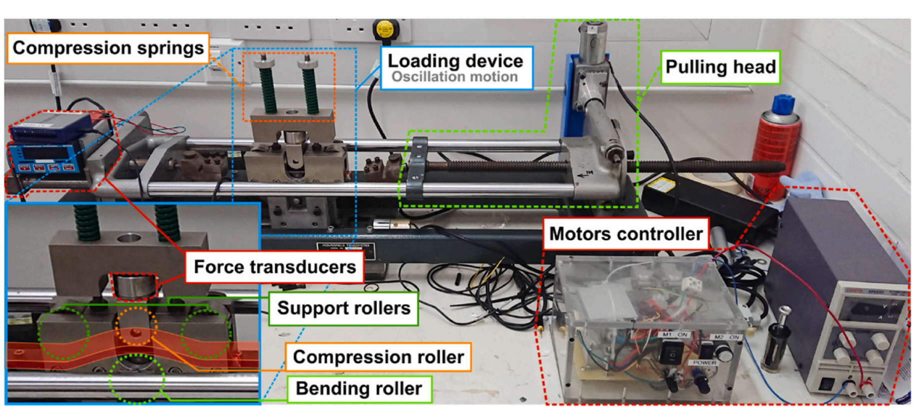

Fig. 3. Experimental testing rig of tension under cyclic bending (TCB) and tension under cyclic bending and compression (TCBC) processes with more details given in Ref. [19].

2. Experimental testing

2.1. Tensile under cyclic bending (TCB) and with additional compression (TCBC) tests

Fig. 3 shows the dedicated TCBC machine used to conduct the TCB and TCBC testing of the test samples with more details given in Ref. [19]. The localised bending was generated by an adjustable bending roller and 2 fixed support rollers. The compressive force was applied by a compression roller through springs. The speeds for tensile elongation and cyclic tool motion were fixed at 2 mm/min and 2 mm/s, respectively. The bending depth and compression force were chosen as variables to control and evaluate the effect of bending radius and compression.

The dimensions of a specimen were used according to the ASTM-E8 standard. Two thicknesses, i.e., 0.5 mm and 0.7 mm were employed in the tests to compare how the sheet thickness was influenced by the effect of bending and compression extent. Table 1 presents a summary of the values of specimen thickness, bending depth and compression force used in both the TCB and TCBC tests. The distance between the support rollers (120 mm) were larger than the gauge length of the sample (80 mm). This minimised the effect of bending on the support rollers. In the case of the TCB test, the compression roller was removed.

For the TCBC test, it was necessary to keep a constant initial bending and position on the sample piece. In the beginning, the specimen was initially clamped at the fixed end of the force transducer. Then, the bending and compression roller was put in place to apply local deformation and squeezing around the middle of the test sample. With one end of the sample clamped, tension was applied by a motor at the other end of the sample at a constant speed. The cyclic bending and compression were generated by the oscillating horizontal motion of the roller subassembly that applies only bending in the case of TCB and bending plus compression in the case of TCBC test conditions. The displacement of the pulling head at fracture was measured as the maximum elongation.

2.2. Single point (SPIF) and double-sided incremental forming (DSIF) processes

Two samples of grade 1 pure Ti with a hyperbolic shape were made in both the SPIF and DSIF processes using a dedicated DSIF machine [9]. Fig. 4a shows the experimental setup of the DSIF machine, fixtures and the arrangement of both tools. The sheet size was 140 mm × 140 mm, and the thickness was 0.7 mm. The radius of the hemispherical tool was 5 mm and the step size was 0.25 mm. The hyperbolic shape was formed with a wall angle starting from 22° and ending at 80° with a cone opening diameter of 90 mm as shown in Fig. 4b. The desired forming depth was 40 mm to achieve a maximum wall angle of 80°. The test was terminated till fracture occurred or the defined depth was reached. The toolpaths were produced using a MATLAB code and the feed rate was 800 mm/min. Rocol Ltd cutting compound was applied on both sides of the clamped sheet for lubrication.

Table 1
Experimental designs of tensile under cyclic bending (TCB) and ensile under cyclic bending and compression (TCBC) of Pure Ti grade 1 samples. The compression roller set will be removed under tensile under cyclic bending (TCB) condition.

No.	Thickness (mm)	Bending depth (mm)	Compression force (N)
1	0.5	4.5	0
2	0.5	4.5	400
3	0.5	4.5	900
4	0.5	7	400
5	0.5	7	900
6	0.5	9	400
7	0.5	9	600
8	0.5	9	900
9	0.7	4.5	0
10	0.7	4.5	400
11	0.7	4.5	900
12	0.7	9	400
13	0.7	9	900

3. Modification of Gurson-Tvergaard-Needleman (GTN) damage models

The fracture strain predicted by the original GTN model was monotonically decreased as stress triaxiality increases [33]. This indicates the inability of correct predictions to the shear and compression and a need of improvement to capture the shear mechanism in ISF more precisely. Bai and Wierzvicki [34] calibrated the fracture strain with extensive experimental testing using butterfly specimens to cover a wider range of stress states. The Lode angle parameter was introduced as another dimension of the deviatoric stresses to indicate the shear effect in accurate mapping of stress states associated with stress triaxiality. The stress triaxiality η and the Lode angle parameter ξ are defined in the following:

$$\boldsymbol{S} = \boldsymbol{\sigma} - \sigma_m \bullet \boldsymbol{I} \tag{1}$$

$$p = \sigma_m = \frac{1}{3} tr(\boldsymbol{\sigma}) \tag{2}$$

$$q = \sigma_{eq} = \sqrt{\frac{3}{2}\boldsymbol{S}:\boldsymbol{S}} \tag{3}$$

$$\eta = \frac{\sigma_m}{\sigma_{eq}} \tag{4}$$

$$r = \left(\frac{9}{2}\boldsymbol{S}\bullet\boldsymbol{S}:\boldsymbol{S}\right)^{\frac{1}{3}} = \left(\frac{27}{2}J_3\right)^{\frac{1}{3}} \tag{5}$$

$$\xi = \left(\frac{r}{q}\right)^3 = \frac{27}{2}\left(\frac{J_3}{\sigma_m^3}\right) \tag{6}$$

where $\boldsymbol{\sigma}$ and $\boldsymbol{S}$ are the stress and deviatoric stress tensor, σ_m and σ_{eq} are the mean stress and the equivalent von Mises stress, respectively. $tr(\boldsymbol{\sigma})$ is the trace of stress tensor. $\boldsymbol{I}$ is the second order identity tensor. J_3 is the third stress invariant.

This study aims to develop a new modified GTN model based on the extension of Zhou et al. [35], which uses the fracture strain surface in the space of stress triaxiality and Lode angle parameter to calibrate the shear damage and its influence on material yielding and void evolution. The new GTN damage model is implemented through the VUMAT user subroutine in Abaqus/Explicit and validated by the TCB and TCBC tests, and the SPIF and DSIF experiments. The original GTN model with the Nahshon-Hutchinson's shear mechanism [36], which was reported to be successful on damage prediction in SPIF [37], was implemented for the comparison. The new GTN model were used to capture the evolution of damage at the different locations and deformation stages, thus to evaluate the determinative process factors on the formability.

3.1. Original Gurson-Tvergaard-Needleman (GTN) model

The concept of the GTN model is to combine the plastic flow equation with the void growth. The yield function in its original form is:

$$\Phi = \left(\frac{\sigma_{eq}}{\sigma_Y}\right)^2 + 2q_1 f^* \cosh\left(\frac{3q_2\sigma_m}{2\sigma_Y}\right) - \left[1 + (q_1 f^*)^2\right] = 0 \tag{7}$$

where q_1, q_2 are GTN model constants suggested to be $q_1 = 1.5, q_2 = 1$ by Tvergaard and Needleman [38]; f^* is equivalent void volume fraction; σ_Y is the yield stress of the undamaged material. The effective void volume fraction f^* is a function of porosity evolution and coalescence

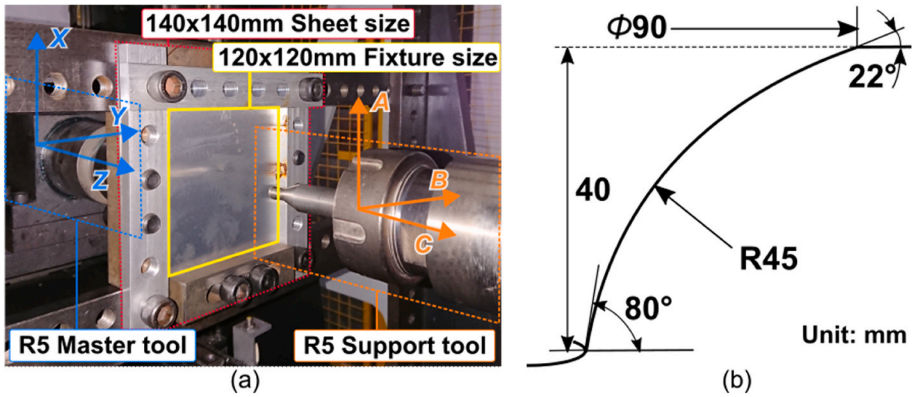

Fig. 4. Experimental setup for single point incremental forming (SPIF) and double-sided incremental forming (DSIF) with more details given in Ref. [9]. (a) The dedicated 6-axis incremental sheet forming machine, and (b) geometry of the desired shape.

stages, which is characterised as in the following form:

$$f^* = \begin{cases} f, if\ f < f_c \\ f_c + \dfrac{\frac{1}{q_1} - f_c}{f_f - f_c}(f - f_c), if\ f \geq f_c \end{cases} \tag{8}$$

where f_c and f_f are the critical and final void volume fractions, respectively, which can be determined by in-situ tests. The void volume fraction f is consisted of two parts: void growth f_{growth} and nucleation $f_{nucleation}$. The commonly used increment laws by Gurson [39] and Tvergaard and Needleman [38] are:

$$\dot{f} = \dot{f}_{growth} + \dot{f}_{nucleation} \tag{9}$$

$$\dot{f}_{growth} = (1 - f)\dot{\varepsilon}^p_{kk} \tag{10}$$

$$\dot{f}_{nucleation} = \frac{F_N}{s_N\sqrt{2\pi}} exp\left[-\frac{1}{2}\left(\frac{\overline{\varepsilon}^p_M - \varepsilon_N}{s_N}\right)^2\right]\dot{\overline{\varepsilon}}^p_M \tag{11}$$

where the $\dot{\varepsilon}^p_{kk}$ is the trace of the plastic strain rate tensor; F_N is the total potential void volume fraction for nucleation; ε_N and S_N are the average value and standard deviation in the normal distribution of the nucleation strain; $\overline{\varepsilon}^p_M$ and $\dot{\overline{\varepsilon}}^p_M$ the equivalent plastic strain and its rate.

3.2. Zhou's shear mechanism

The modification to inherent limitations of the GTN model under low stress triaxiality was proposed by several researchers [36,40,41]. These studies revealed the difficulty of integrating the shear damage in the form of void volume fraction increment to correctly capture the shear effect in material yielding and its subsequent evolution of voids. Zhou et al. [35] refined the yield function, focusing on the shear effect in material softening instead of void growth. The shear damage was separated from the void evolution mechanisms as an independent variable and presented in a phenomenological form based on fracture strain loci from experimental tests. A successful application was conducted in the fracture prediction in spinning process [42], which included through-thickness shear and compression. The plastic flow potential equation is incorporated with shear damage into the following form:

$$\Phi = \left(\frac{\sigma_{eq}}{\sigma_Y}\right)^2 + 2q_1 f^* \cosh\left(\frac{3q_2\sigma_m}{2\sigma_Y}\right) - \left[1 + (q_1 f^* + D_s)^2 - 2D_s\right] = 0 \tag{12}$$

where D_s is the shear damage variable. When $D_s = 0$, the function degenerates to the original GTN model. Assume the plastic strain for shear fracture is denoted as ε^s_f, D_s can be presented as a ratio of the equivalent plastic strain $\overline{\varepsilon}^p_M$ and shear fracture strain ε^s_f, which can be written as:

$$D_s = \left(\frac{\overline{\varepsilon}^p_M}{\varepsilon^s_f}\right)^{n_s} \tag{13}$$

where n_s is a power constant greater than one, which alters the shear damage evolution speed. Differentiation of Equation (13) gives:

$$\dot{D}_s = n_s \bullet \left(\frac{\overline{\varepsilon}^p_M}{\varepsilon^s_f}\right)^{n_s - 1} \frac{\dot{\overline{\varepsilon}}^p_M}{\varepsilon^s_f} \tag{14}$$

Applying a weight function $\psi(\eta, \xi)$:

$$\dot{D}_s = \psi(\eta, \xi) \bullet n_s \bullet \left(\frac{\overline{\varepsilon}^p_M}{\varepsilon^s_f}\right)^{n_s - 1} \frac{\dot{\overline{\varepsilon}}^p_M}{\varepsilon^s_f} \tag{15}$$

where the weight function $\psi(\eta, \xi)$ was defined as:

$$\psi(\eta, \xi) = \begin{cases} g_0, \eta > 0 \\ g_0(1 - k) + k, \eta \leq 0 \end{cases} \tag{16}$$

In the above equation, g_0 can be presented by any Lode dependency function and k is a weight factor to adjust the effect of negative stress triaxiality. The fracture strain were interpolated based on the experimental data from Gatea [43] and Zhai et al. [44], and implemented in the model by the fitting equation.

The total damage can be given as an entity involving both void and shear damage:

$$D = q_1 f^* + D_s \tag{17}$$

3.3. Modified void evolution function

The existing nucleation mechanism in the original GTN model gave an averaged distribution of all potential second phase for nucleation only considering the void interactions without shear effects, as presented in Equation (11). Considering shear condition in nucleation process, Malcher et al. [41] introduced a Lode-dependent function in combination of Nahshon and Hutchinson's shear mechanism [36] as in the following form:

$$\dot{f}_{nucleation} = (g_0^2) \bullet \frac{f_N}{s_N\sqrt{2\pi}} exp\left[-\frac{1}{2}\left(\frac{\overline{\varepsilon}^p_M - \varepsilon_N}{s_N}\right)^2\right]\dot{\overline{\varepsilon}}^p \tag{18}$$

3.4. Modified shear weight function

Experimental and RVE model results [45,46] suggested that the void volume fraction evolution was significantly dependent on the initial void volume fraction and the increasing influence of the Lode angle effect with the decrease of stress triaxiality. Incorporating the modification by Malcher et al. [41] and the asymmetric Lode function by Dæhli et al. [45] validated in RVE model, the Lode dependency function is reconstructed:

$$g_0 = \frac{1}{2} \bullet [1 + \cos(3\theta_L)] = \frac{1}{2} \bullet (1 - \xi) \tag{19}$$

$$\psi(\eta, \xi) = \begin{cases} f^{q_4} \bullet \left(1 - g_0^2\right)^{\frac{1}{|\eta|+k}}, \eta_{lim}^{(-)} \le \eta \le \eta_{lim}^{(+)} \\ 0, \eta > \eta_{lim}^{(+)} \; or \; \eta < \eta_{lim}^{(-)} \end{cases} \tag{20}$$

In the weight function $\psi(\eta, \xi)$, the void volume fraction exponent is for idealised cell structure, where $q_4 = 1/2$ for 2D and $q_4 = 1/\,3$ for 3D problems [40]. θ_L is the Lode angle. k is a weight factor to adjust the Lode angle effect with offset of stress triaxiality. Two cut-off values of stress triaxiality $\eta_{lim}^{(+)}$ and $\eta_{lim}^{(-)}$ are set in the weight function as a criterion of the void closure and coalescence [46] to improve computing efficiency.

3.5. Implementation of the shear modified Gurson-Tvergaard-Needleman (GTN) model

The framework of the GTN model via Abaqus VUMAT user subroutine is based on the study of Gatea et al. [43], which was proven to be suitable for SPIF process simulation and damage prediction. The plastic strain computation is calculated by a returning mapping algorithm. The adaption is made for the modification of damage variables in terms of damage and void evolution calculated and accumulated in solution dependent variables (SDV). The detailed procedure for the implementation may be referred to Refs. [43,47].

4. Finite element (FE) modelling

FE simulations were used to capture the evolutions of the stresses and damage due to local bending, compression and un-bending deformation at different locations through thickness. This provides an opportunity to establish the relationship between the process parameters and strain evolution and stress states. Such a relationship also allows correlation between the phased stress state and damage evolution to reveal the underlying mechanisms of fracture occurrence and formability improvement.

4.1. Tensile under cyclic bending (TCB) and with compression (TCBC) tests

Two FE models were separately established for the 0.7 mm thick grade 1 pure Ti sample. A 4.5 mm bending depth was used for both the TCB and TCBC tests with a 400 N compression force applied in the case of TCBC. C3D8R brick elements were used to generate the mesh with 4 layers through thickness and improved mesh density from element size of 0.5 mm in the area under TCB and TCBC loading of the oscillating roller motion and 1.5 mm in the remaining area of the test specimen. All rollers including the support, bending and compression rollers were defined as analytical rigid shell part. For the TCBC test, Abaqus Connector elements of CONN3D2 (slot + align) were used to connect the compression roller to apply a constant force. The bending depth was applied in step 1 to give an initial bending on the specimen, followed by the tension applied in the lateral direction and oscillating bending in step 2. To improve the computational efficiency, mass scaling was applied with a minimum increment time of $1 \times 10^{-5}\, s$. Because of the use of rotating rollers in the TCB and TCBC tests, friction between the specimen and all the rollers are negligible. The interface between the specimen and all rollers was defined to be frictionless.

The material properties of grade 1 pure Ti were used from uniaxial tensile tests and study by Gatea et al. [21]. All material and damage model parameters are listed in Table 2. $q1, q2, q3$ are GTN model constants and ε_N, S_N and F_N are void nucleation coefficients of material that determined by in-situ test by Gatea [43]. k is the calibration factor of stress triaxiality on the Lode function for void nucleation [41]. n_s is the parameter to calibrate the soften effect at the early stage of plastic deformation [35]. k_w is the parameter to control the shear damage rate. k, n_s and k_w were calibrated by benchmarking of uniaxial tensile tests based on force-displacement relationship and elongation until fracture, where the values achieve the best accuracy would be selected. $\eta_{lim}^{(-)}$ and $\eta_{lim}^{(+)}$ are stress triaxiality limits to define the boundary of fracture strain surface and improve the calculation efficiency. E, ν are the Young's modulus and Poisson's ratio, respectively. A, B and n are parameters for the Johnson-Cook's constitutive model obtained through the flow stress curves by tensile tests.

Table 2
Material and Gurson-Tvergaard-Needleman (GTN) model parameters being used in the finite element (FE) simulation [21].

E (MPa)	ν	A (MPa)	B (MPa)	n	q_1	q_2	q_3
105,000	0.34	170	356	0.53	1.5	1	2.25
f_f	f_c	ε_N	S_N	F_N	q_4	k	n_s
0.3025	0.2593	0.3	0.2	0.017	1/3	0.2	1.2
$\eta_{lim}^{(-)}$	$\eta_{lim}^{(+)}$	k_w					
−1	1	1.4					

4.2. Single point (SPIF) and double-sided incremental forming (DSIF) processes

Fig. 5 shows the schematic of SPIF and DSIF modelling. The sheet material was fully fixed at the flange region and adapted to a clamping size of 120 mm × 120 mm x 0.7 mm. The contact property was defined by surface-to-surface contact with a coefficient of friction of 0.05, which was estimated from the force measurement. The toolpaths defined on the master and support tools were processed to repeat the practical positioning during the experimental tests to improve the prediction accuracy.

The blank sheet was divided into 4 parts and applied with element sizes of 3 mm, 0.75 mm, 0.25 mm and 1.5 mm from edge to centre. 4 layers of C3D8R elements were created through the sheet thickness with a total of 45,280 elements. The minimum incremental length was limited by a mass scaling of $2 \times 10^{-5}\, s$. Both the original GTN with Nahshon-Hutchinson's shear mechanisms and the new GTN model were implemented for comparison. The Nahshon-Huchinson's shear mechanisms can be concluded in the following equation [36]:

$$\dot{f}_{shear} = \frac{k_w f(1-\xi)}{\sigma_m} \boldsymbol{S} : \boldsymbol{d\varepsilon^p} \tag{21}$$

$$\dot{f} = \dot{f}_{growth} + \dot{f}_{nucleation} + \dot{f}_{shear} \tag{22}$$

where k_w is the parameter to control the shear damage rate. $\boldsymbol{d\varepsilon^p}$ is the plastic strain rate tensor. The FE simulations were conducted using ABAQUS/Explicit package.

5. Evaluation of deformation and fracture

5.1. Forming forces and formability improvement

The forming forces recorded in the uniaxial tensile test, the TCB and TCBC tests of 4.5 mm bending depth and 400 N compression force versus displacement are plotted in Fig. 6. It was observed that the tensile force was reduced from both the TCB and TCBC tests. However, further reduction of forming forces in the TCBC was insignificant, which was different from the cases with the tests of AA5251 [19].

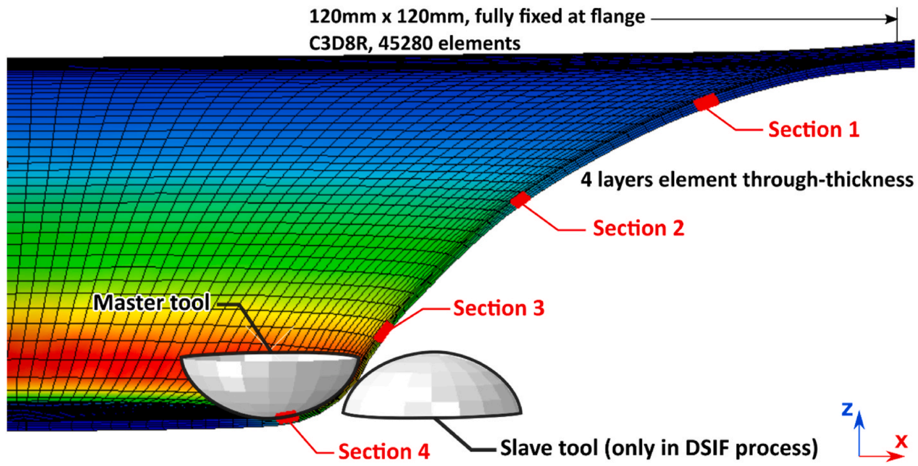

Fig. 5. Schematic of finite element modelling and the investigated sections for single point (SPIF) and double-sided incremental forming (DSIF) processes.

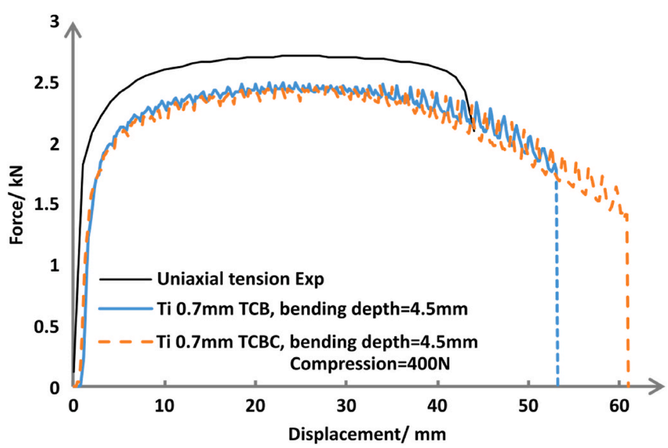

Fig. 6. Tensile forces comparison from uniaxial tensile, tension under cyclic bending (TCB) and tension under cyclic bending and compression (TCBC) tests for grade 1 pure Ti 0.7 mm.

5.2. *Effect of bending depth and compression force on elongation-to-fracture in tensile under cyclic bending (TCB) and tensile under cyclic bending and compression (TCBC) tests*

The fractured samples by uniaxial tensile, the TCB and TCBC tests were shown in Fig. 7. Of all the samples, the fractures were similar to the rapture from uniaxial tension, in which the section of failure was at an angle to the tensile direction. The reduction of sample width was uniformly distributed over the deformation region. On surface appearance, there was smooth trace of roller contact and compression in both the TCB and TCBC samples. However, there were no apparent micro-cracks caused by cyclic bending from the grade 1 pure Ti samples, as compared to the AA5251-H22 sheets reported by Ai et al. [19].

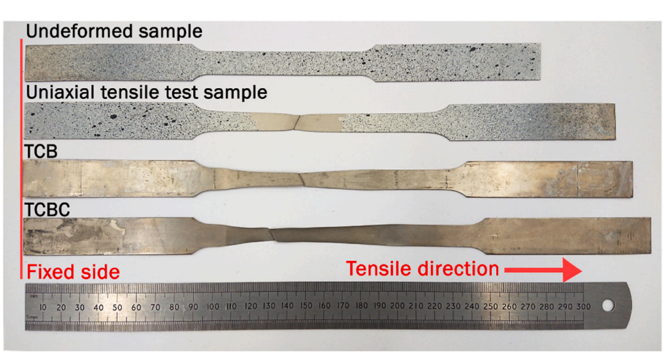

Fig. 7. Completed testing samples for comparison in uniaxial tensile, tensile under cyclic bending (TCB) and tensile under cyclic bending and compression (TCBC) tests.

The maximum elongation results from the TCB and TCBC tests were plotted in Fig. 8 at different test conditions. Both the TCB and TCBC tests achieved over 40% larger elongation than that obtained from the uniaxial tensile testing. However, the changes of testing parameters, especially the compression force, was more effective on the 0.5 mm thick specimens. When the test samples formed with a bending depth of 9 mm and compression force of 900 N, the 0.5 mm thick sheet achieved 73 mm elongation-to-fracture exceeding the 70.5 mm elongation of the 0.7 mm thick specimen. Similar results were reported for AA5251-H22 and AA6082-T6 materials that increasing sheet thickness brought limited maximum elongation [19]. For grade 1 pure Ti sheets, the formability improvement by bending depth was less under high bending depth or compression, whereas for AA5052-H22 or AA6022-T4 sheets, the elongation-to-fracture were decreased by excessively large bending depth [19,28]. These results indicate the reduced effect of formability improvement by compression on thicker specimens, as well as a negative effect due to excessive bending.

The different effects of bending depth, thickness and compression on the process formability can be attributed to the deformation modes during local contact period in TCB and TCBC. Fig. 9 illustrated two deformation stages, bending and reverse-bending (or unbending), and their stress and strain diagrams. In the bending stage, the material starts to be deformed to curvature where the convex and concave sides are under tension and contact pressure, respectively. The various elongations through thickness generates a difference in longitudinal strain $\Delta\varepsilon$. $\Delta\varepsilon$ is balanced in the reverse-bending stage, where the concave side, previously in contact with the bending tool, is under tension without contact pressure. Such switchover of cyclic deformation modes by tools contact results in varied stress states and damage accumulation along thickness direction that determines the initiation of the final fracture.

The compression independently superimposes on the through-thickness compression that reduces the void growth in the bending stage. This increases the through-thickness stress σ_t and reduce the longitude stress to yielding σ_s in TCBC process, according to Tresca's yield criterion. Thus, the tension T in TCBC is smaller than it in TCB case.

It can be deduced that both the increased thickness and the reduced bending radius result in a larger through-thickness strain discrepancy $\Delta\varepsilon$, and the contact pressure in the bending stage. This leads to increased deformation in the reverse-bending stage, whose stress state is not affected by any parameters. This explains why a larger formability enhancement is achieved in the tests with a smaller thickness of samples.

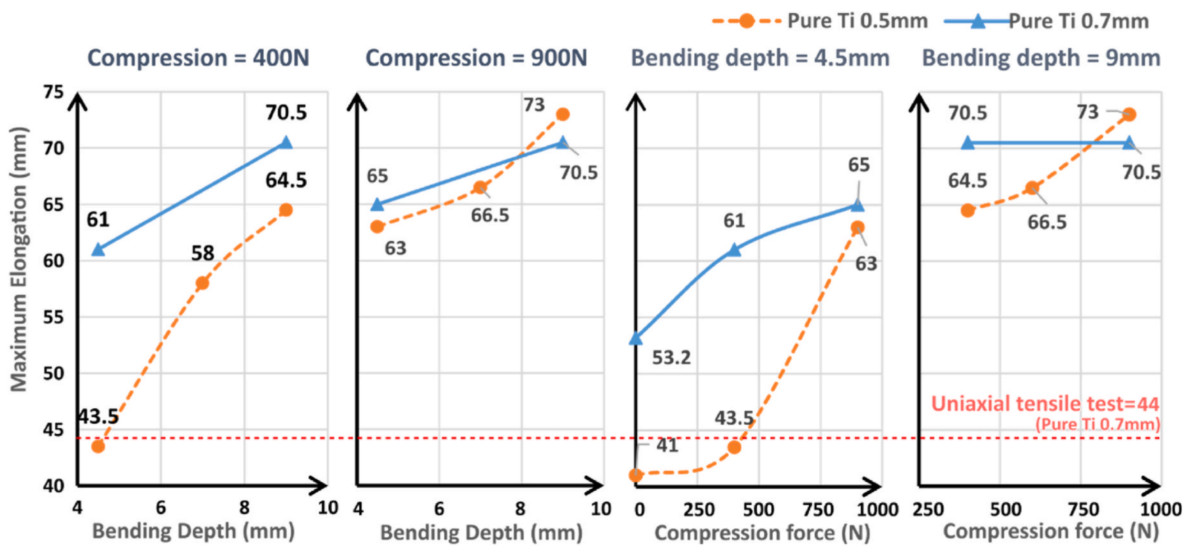

Fig. 8. Maximum elongations obtained under various bending depths and compression forces in tensile under cyclic bending (TCB) and tensile under cyclic bending and compression (TCBC) tests. The zero-compression force refers to tensile under cyclic bending test condition.

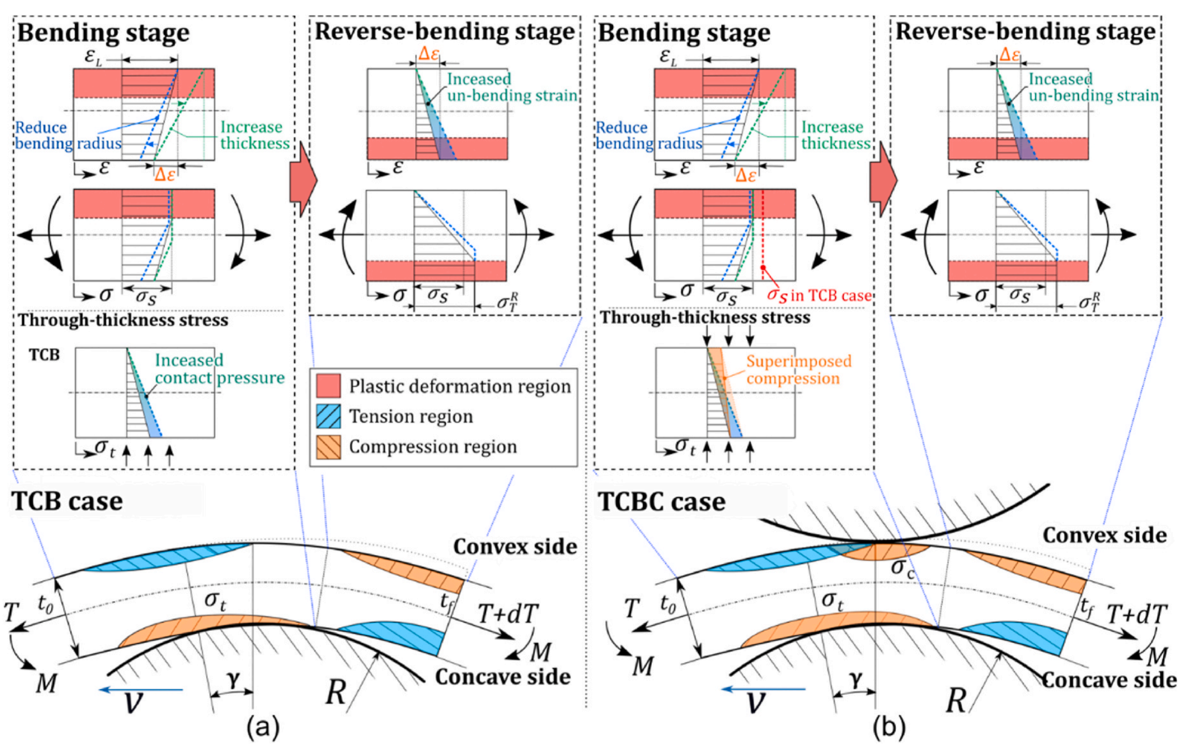

Fig. 9. Schematics of the stress and strain distribution through thickness in the bending and reverse bending stages. (a) Tensile under cyclic bending (TCB) case, and (b) tensile under cyclic bending and compression (TCBC) case. The effect of changing process parameters is illustrated with dash lines of different colours.

A larger damage accumulation due to reverse-bending deformation offsets the reduction of damage growth by increasing contact pressure, by increasing the bending depth or thickness. Therefore, the stress evolution in the bending stage, and the amount of strain recovery in the reverse-bending stage are determinative factors for elongation-to-fracture in both the TCB and TCBC tests.

5.3. Deformation and damage mechanics

5.3.1. Strain distribution and damage prediction

5.3.1.1. Tensile under cyclic bending (TCB) and with compression (TCBC) tests. The equivalent plastic strain and damage variables obtained from FE simulation were shown in Fig. 10. The length in the tensile direction (X axis in Fig. 10) was scaled by a factor of 0.5 for better presentation. The results of equivalent plastic strain (PEEQ) suggested that a uniformed distribution of plastic deformation occurred in TCB and TCBC in the longitudinal direction, which agrees with previously reported experimental strain results in TCB of aluminium alloys [28,31]. As a

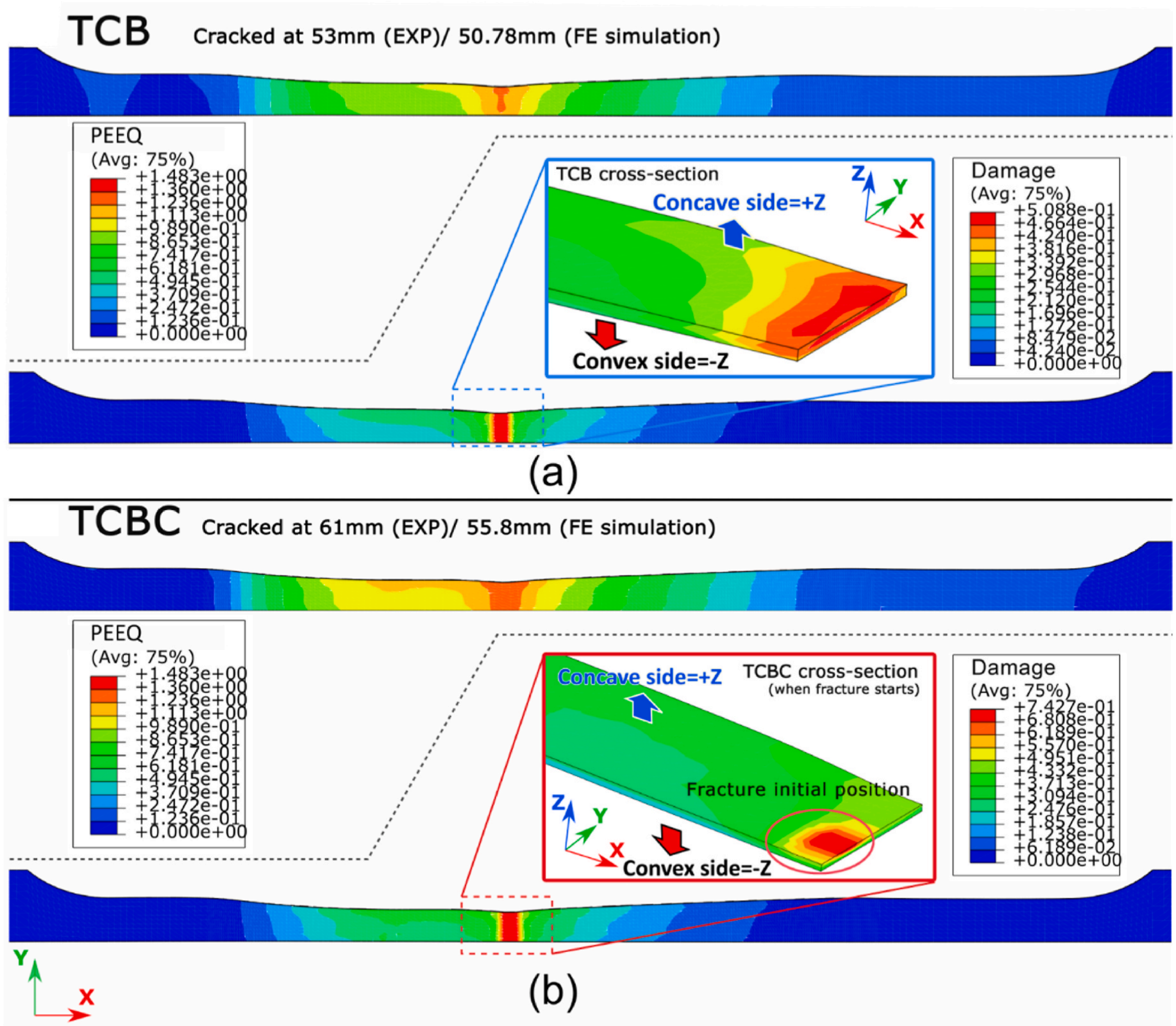

Fig. 10. Distribution of equivalent plastic strain (PEEQ) and damage variable in finite element simulation. (a) Tensile under cyclic bending (TCB), and (b) Tensile under cyclic bending and compression (TCBC).

larger amount of elongation-to-fracture was achieved in TCBC, the plastic deformation was extended to a wider range and reached a higher strain value in the region around fracture location as compared to the case of TCB.

The predicted elongation at fracture for the TCB was 50.8 mm as compared to 53 mm from the TCB test, and 55.8 mm for the TCBC as compared to 61 mm from the TCBC test. It was observed in the cross-section view at the moment before fracture that the fracture initiated on the concave side, the surface in contact with the bending roller, instead of the convex side with or without the compression force applied by the compression roller in the TCBC test. The initial fracture location highlighted the dominant role of the reverse-bending stage, where the most deformation on the concave surface occurs.

5.3.1.2. Single point (SPIF) and double-sided incremental forming (DSIF). The experimental samples of the SPIF and DSIF processes and fracture depth predicted with the comparison of the original and the new modified GTN model are shown in Fig. 11a and b. It can be observed from Fig. 11b that the support tool losing contact in DSIF test. As the toolpaths were defined to match the actual positioning in the experiments, this loss of contact of the support tool was duplicated in DSIF simulation after the tools passing section 2 (Fig. 5). The improved formability indicated by the larger fracture depth was achieved in the DSIF process in experiment. The original GTN model with Nahshon-Hutchinson's shear mechanism gave the earlier facture predictions in both the SPIF and DSIF processes. This may be because the incorporation of the shear damage to the overall void volume fraction would simultaneously accelerate the material softening and damage, then overestimate the damage accumulation. The fracture initiated at the diagonal direction which matches the experimental results of SPIF as shown in Fig. 11c. Meanwhile, Fig. 11d shows the new modified GTN model correctly predict of fracture depth for both the SPIF and DSIF processes, whilst only the fracture location in the DSIF case was identical to the experiment.

Fig. 12 present the comparisons of equivalent strain and damage prediction obtained by the original and the new modified GTN models. The equivalent strain results shown in Fig. 12a and b indicate that similar strain predictions were obtained from both SPIF and DSIF cases. However, the different responses to stress states in SPIF and DSIF simulation led to diverged estimations to damage variables as plotted in Fig. 12c and d, whereas the new GTN model presents more accurate damage prediction of both the SPIF and DSIF processes.

In the through-thickness direction, the fracture initiates on the surface opposite to the master tool contact (convex side) in both the SPIF and DSIF processes. The predicted fracture position agrees with the previous experimental and analytical study in both SPIF by Fang et al. [14] and DSIF by Lu et al. [9]. The different fracture locations in the TCB, TCBC tests as compared to the SPIF and DSIF processes suggest a distinction in deformation mechanisms between uniaxial and biaxial bending-under-tension and compression.

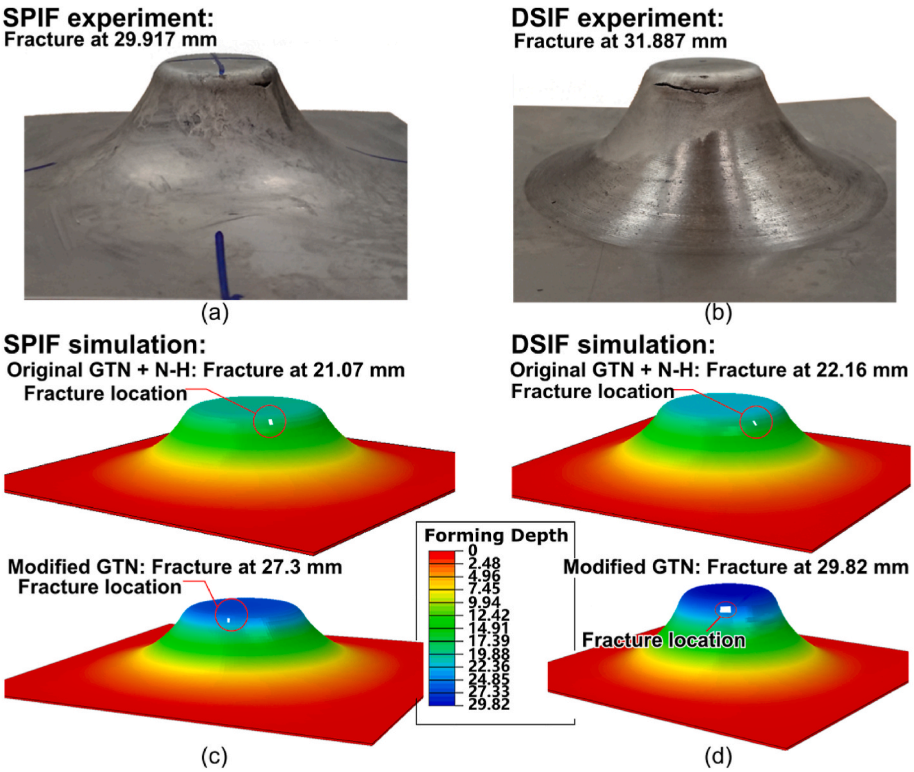

Fig. 11. Experimental and finite element simulation results with two Gurson-Tvergaard-Needleman (GTN) models. Completed test samples of grade 1 pure Ti using (a) single point incremental forming (SPIF) and (b) double-sided incremental forming (DSIF), and the comparisons of damage predictions between the original Gurson-Tvergaard-Needleman model with the Nahshon-Hutchinson's shear mechanisms and the new modified Gurson-Tvergaard-Needleman model in (c) single point incremental forming (SPIF) and (d) double-sided incremental forming (DSIF).

5.3.2. Localised deformation and characteristics

5.3.2.1. Tensile under cyclic bending (TCB) and with compression (TCBC) tests. Localised bending-under-tension reduces the tension required for material yielding in the tensile direction, which reduces the forming forces and limits the plastic deformation only occurring in the contact region driven by tools contact [14,19,27]. Due to the longitudinal elongation of the sample, the stroke range for the bending and support rollers would result in a smaller area of deformation under both TCB and TCBC conditions. The deformation zones could be divided by the number of contacts with the bending roller. The maximum principal strain of the TCBC specimen is plotted on the undeformed sample with the number of bending roller oscillation cycles as shown in Fig. 13a. The contour plot suggests that the maximum principal strain reached the highest level in section 2 with the forming cycles above 40 times. This conclusion is confirmed by the equivalent plastic strain history of different sections of the sample plotted in Fig. 13b. The material in sections 3 and 4 exited the range of cyclic tool stroke after a certain amount of elongation, which showed that the plastic strain levelled after this section moved out of the contact region of the roller frame by certain displacement. The localised deformation feature prevented the strain concentration as normally occurred in the uniaxial tensile test and led to homogenised damage in both the TCB and TCBC samples.

5.3.2.2. Single point (SPIF) and double-sided incremental forming (DSIF). The incremental strain evolution against forming depth from simulations of the SPIF and DSIF processes is plotted in Fig. 14 based on four sections defined in Fig. 5. Unlike the continuous increase throughout the TCB and TCBC tests, the equivalent strain increases in a specific range of forming depth in both the SPIF and DSIF processes when the tool passes on a particular section. The squeezing effect between the master and support tools in the DSIF leads to extensive material thinning and the larger strain value than that in the SPIF at the beginning of forming process (Section 1). In sections 2-4, the final strain values obtained from both SPIF and DSIF processes are close. The effective strains from DSIF were larger than them in SPIF in sections 3 and 4, even the support tool already losing contact that caused the DSIF degenerated to SPIF processes.

The equivalent strain evolution shows that the SPIF and DSIF processes are under localised bending-under-tension and plus compression conditions with limited cycles. In the direction of major strain growth, the incremental deformation is "discrete" in SPIF and DISF in contrast to the "continuous" mode in TCB and TCBC processes. In the DSIF process, the additional compression only applies on a limited number of forming cycles, depending on the relative tool positions, to affect the damage history during double-contact period as compared to the SPIF process. Thus, the relative tool position is an influential factor to fracture but cannot be reflected in the TCBC process. The formability differences due to relative tool positions have been confirmed in experimental studies [9].

5.3.3. Stress states during localised deformation

5.3.3.1. Tensile under cyclic bending (TCB) and with compression (TCBC) tests. To further investigate the deformation evolution and through-thickness bending in different stages, the stress state variation in the thickness direction was analysed. Fig. 15 shows the relative increases of the equivalent plastic strain, stress triaxiality and damage evolutions before, during and after contact based on four layers of elements in the thickness direction in section 2, the part experienced the most deformation cycles (Fig. 12). The X-axis was relative "time" when the contact starts at $x = 0$. The whole contact duration is indicated in the shadow area. The variables were magnified and presented in a form of accumulation. In a single tool contacting period, the equivalent plastic strain increase in the TCBC was larger than that in the TCB except in the concave layer, which is on the side contacting to the bending tool (Fig. 15a and b). The strain on the concave side increases after the contact period indicating a rebalance of through-thickness strain discrepancy in the reverse-bending stage. It is noted that the plastic strain increment in the concave layer in a single deformation period was almost identical between the TCB and TCBC tests because the reverse-bending stage is not affected by the stress states but by the thickness

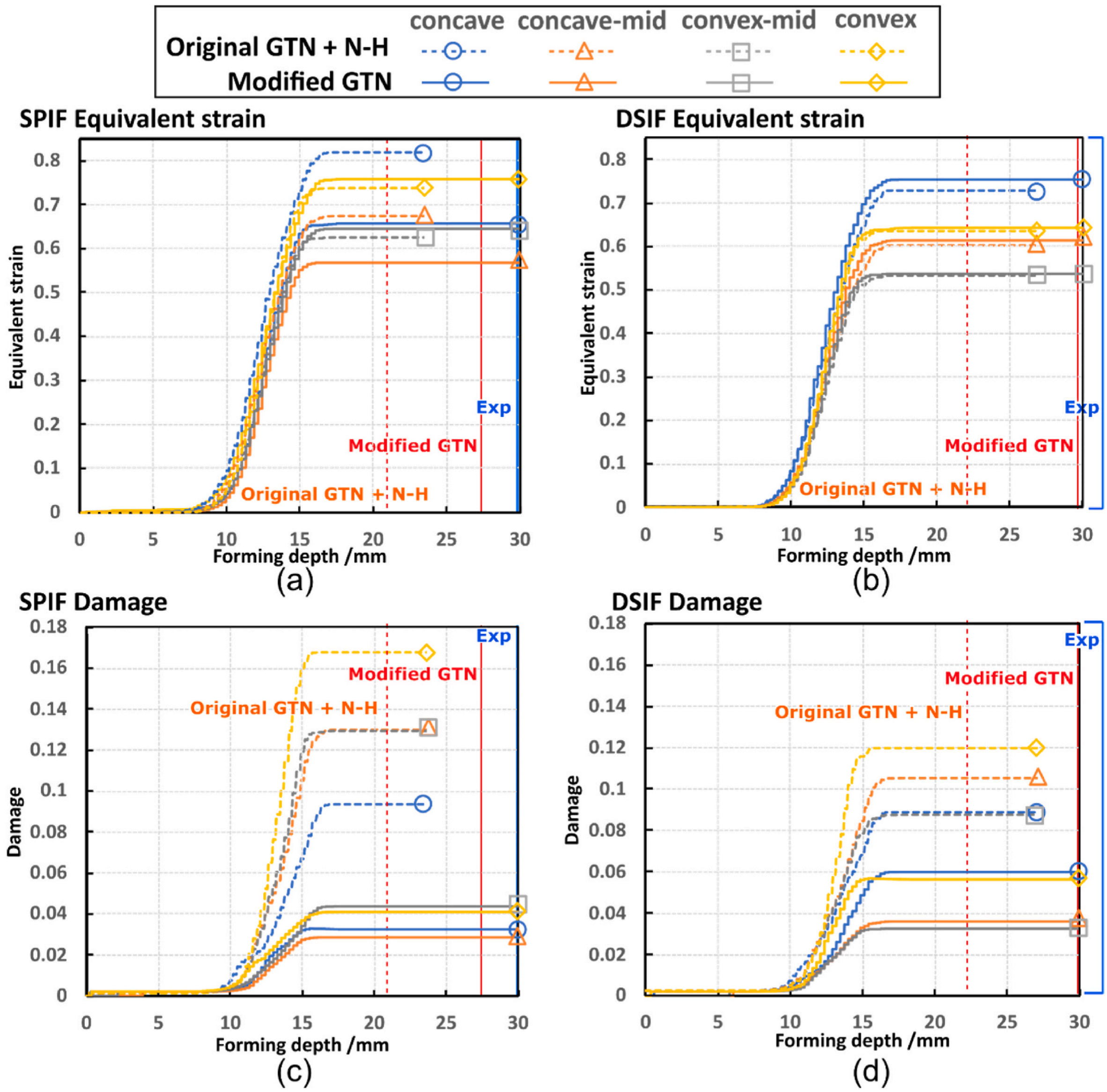

Fig. 12. Comparisons of equivalent strain evolutions and damage predictions in finite element simulations using the original Gurson-Tvergaard-Needleman (GTN) model with the Nahshon-Hutchinson's (N–H) shear mechanisms and the new Gurson-Tvergaard-Needleman (GTN) model. Equivalent strains on through-thickness layers in (a) single point incremental forming (SPIF) and (b) double-sided incremental forming (DSIF), and damage prediction in (c) single point incremental forming (SPIF) and (d) double-sided incremental forming (DSIF).

and bending depth.

The stress triaxiality η evolution plotted in Fig. 15c and d shows the tool contact and bending effect from the stress point of view. The tool contact reduces the stress triaxiality in the concave layer while the deformation in the intermediate layers remained relatively constant. In the case of TCBC (Fig. 15d), the additional compression brought in a further reduction of stress triaxiality in all layers.

The damage evolution on the concave side was higher than the convex side after a single contact duration as shown in Fig. 15e and f. Therefore, it can be concluded that the reverse-bending leads to more damage accumulation, which is the reason for fracture initiation in the concave layer. In the original GTN model, the void growth and nucleation (as presented in Equations (10) and (11)) are proportional to plastic strain increment. However, this trend was reversed in the TCB and TCBC, where a larger amount of deformation hence a higher level of plastic strain led to less damage due to the through-thickness stress states differences in bending-under-tension deformation. The phenomenological calibration through equivalent fracture strain surface and Lode function in the new GTN model gave correct compensations to different stress states in the TCB and TCBC tests and hence improved accuracy of damage prediction.

The paths of the stress state can be plotted using the plane of stress triaxiality and normalised Lode parameter, as proposed by Bai and Wierzbicki [34] and shown in Fig. 16. The stress paths pointed out the key differences of the deformation mode between the TCB and the TCBC. The intermediate layers were under pure tension while the concave layers followed the line of plane stress conditions in the TCB. In the TCBC, there is a trend of a shift beyond the shear state towards axial symmetric compression. This is accompanied with a decrease of stress triaxiality. The comparison between the stress paths of the TCB and TCBC tests clearly shows that the reduced shear effect and increased compression are the reasons for the delay of fracture, especially in the concave layer where the crack is initiated.

5.3.3.2. Single point (SPIF) and double-sided incremental forming (DSIF). The stress state evolutions during the local contact period are critical to

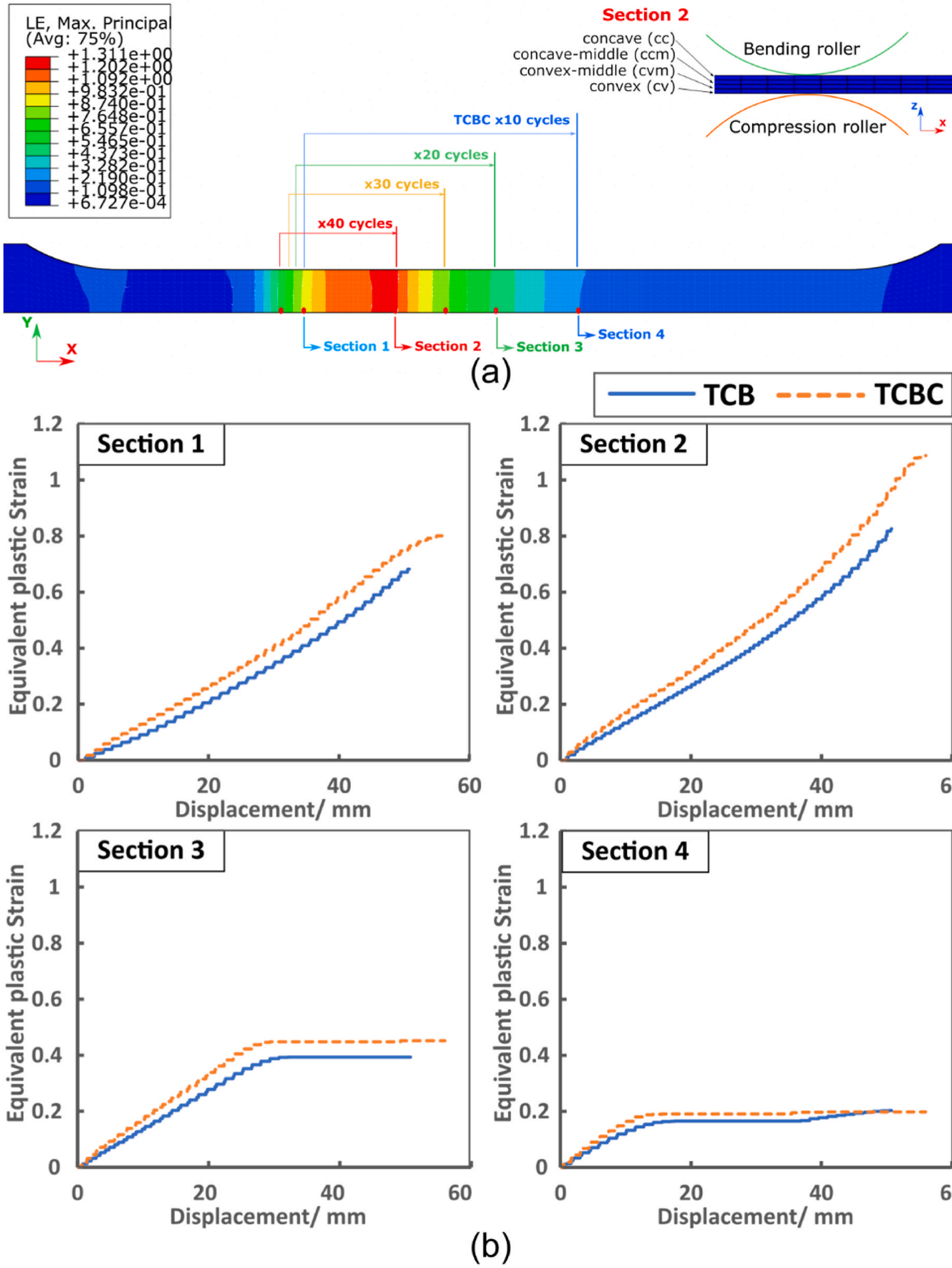

Fig. 13. Maximum principal logarithmic strain (LE) distribution and plastic strain comparisons between tensile under cyclic bending (TCB) and tensile under cyclic bending (TCBC) at different locations in longitudinal directions. (a) Contour plot of longitudinal strain distribution and its relationship with the tool contact times. (b) Comparison of equivalent plastic strain evolutions in tensile under cyclic bending (TCB) and tensile under cyclic bending (TCBC) at sections 1-4.

the damage accumulation as shown in TCB and TCBC analysis (Figs. 15 and 16), which can be captured by the new modified GTN model. The relative equivalent strain growths and the stress triaxiality evolutions in SPIF and DSIF simulations are compared through 4 layers of elements in section 2 as shown in Fig. 17. The reason to use section 2 is that section 2 keeps double contact during the local forming processes. Although sections 3 and 4 are closer to the fracture location, the loss of contact of the support tool in DSIF testing resulted in a degeneration from DSIF to SPIF, which makes the stress states in section 3 and 4 of SPIF and DSIF less comparable to reveal the effect of the support tool. The relative

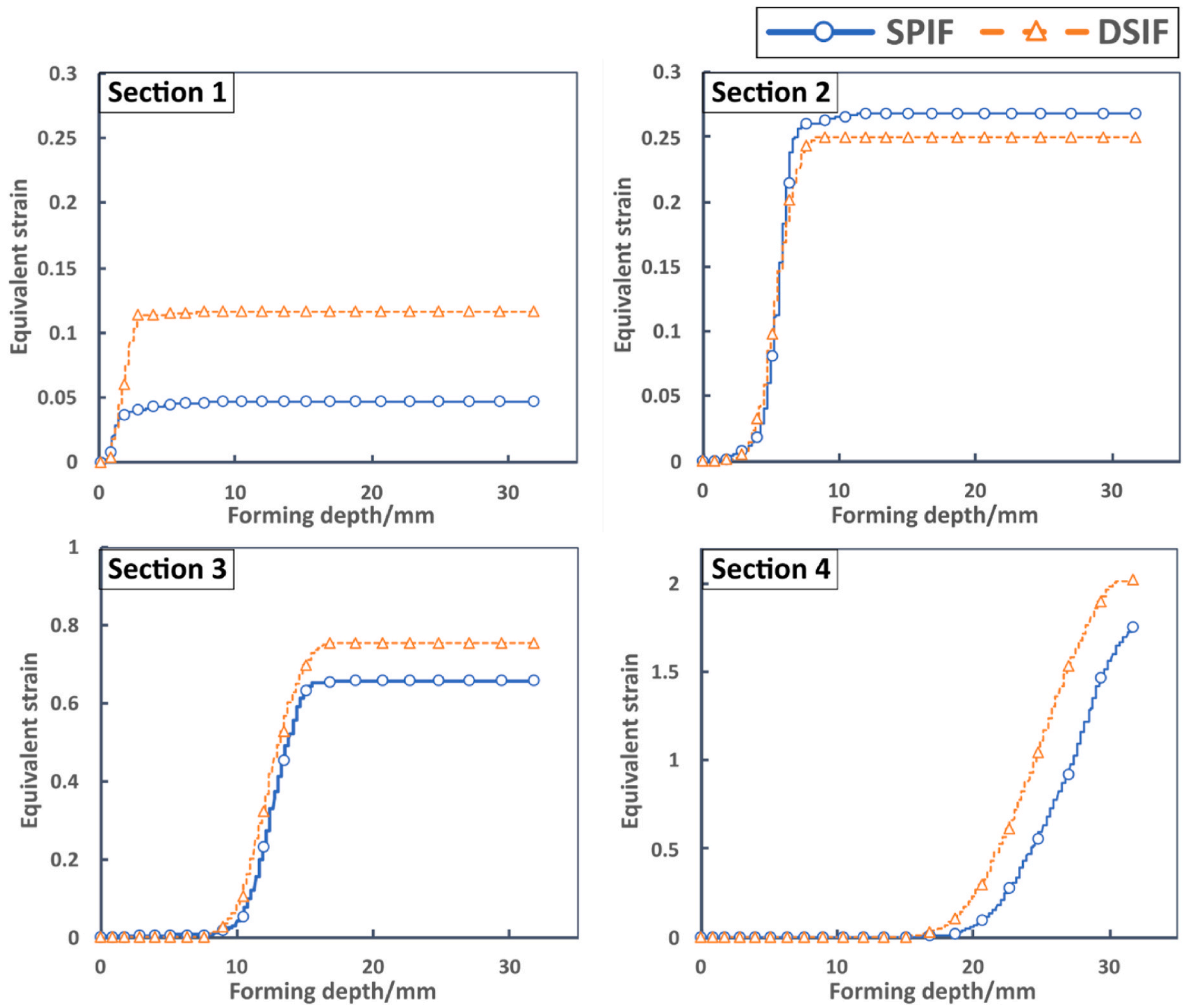

Fig. 14. The comparison of equivalent plastic strain evolutions at section 1-4 in single point incremental forming (SPIF) and double-sided incremental forming (DSIF) processes.

strain increases during a single contact period are almost equal through all layers in the both processes, whereas the after-contact deformation was only occurred on the outer surface (convex layer) in SPIF process (Fig. 17a and b). Fig. 17c and d shows the localised biaxial bending significantly increases the stress triaxiality values in both the SPIF and DSIF processes than that in the TCB and TCBC tests (Fig. 15c and d). Though the stress triaxiality evolutions coincide with the representative stress state behaviours of before, during and after the tool contact, the values and timing of strain increases were largely identical in thickness direction in the ISF cases. Such phenomenon indicates less domination of the reverse-bending in SPIF and DSIF processes as compared to the TCB and TCBC processes. However, the compression applied by the support tool reduced the stress triaxiality in the double-contact region in the DSIF as occurring in the TCBC test, which suggests that the same effect on the formability improvement is achieved by applying the support tool in the DSIF and the compression roller in the TCBC.

There are two major differences between the deformation mechanisms between the TCB and TCBC tests, and the SPIF and DSIF processes. From the process point of view, the strain increment and stress states per contact period in the SPIF and DSIF are determined by the process parameters and the forming geometry. The compression only affects a limited range of plastic deformation in the DSIF process. Fig. 18 shows the stress triaxiality and damage variations in the last 3 tool contact passes. As indicated in Fig. 18a, only the last two passes on tool contact were under double-contact condition. However, Fig. 18b clearly shows a significant declination of the damage growth rate in the double-contact region in DSIF. It is suggested though the period of additional compression is limited, the improvement of formability is still pronounced. The fracture initiation is mainly determined by biaxial tension on the convex surface in both the SPIF and DSIF processes, instead of uniaxial tension combined with shear and compression on the concave surface in the TCB and TCBC tests. This inference is in agreement with the experimental observation and the analytical conclusion [9,14].

The stress paths of the SPIF and DSIF processes of a single local deformation cycle are drawn in the plane of stress triaxiality and Lode angle parameter as shown in Fig. 19. The dot trend lines with starting points of a cross mark and directional arrows are plotted to show the stress state evolution in the localised deformation before, during and after the tool contact duration. The intense biaxial bending from the stress paths in both the SPIF and DSIF processes exhibit a stronger correlation to material position through thickness than the TCB and TCBC tests. In the SPIF process (Fig. 19a), the tool-contacting layers (concave and concave-mid layers) start at plane strain and pure tension states in the bending stage, then transfer along the plane strain deformation path and approach extensive uniaxial tension state in the reverse-bending stage. The lessened bending deformation in the horizontal direction and tool contact pressure on the concave side are the reasons for the reduced stress triaxiality and increased Lode parameter. On the other hand, the material away from tool contact (convex-mid and convex layers) is under compression at the uncontacted stage because of elastic recovery. In this case, the stress state begins with axisymmetric compression and follows a plane strain deformation path, finally reaches

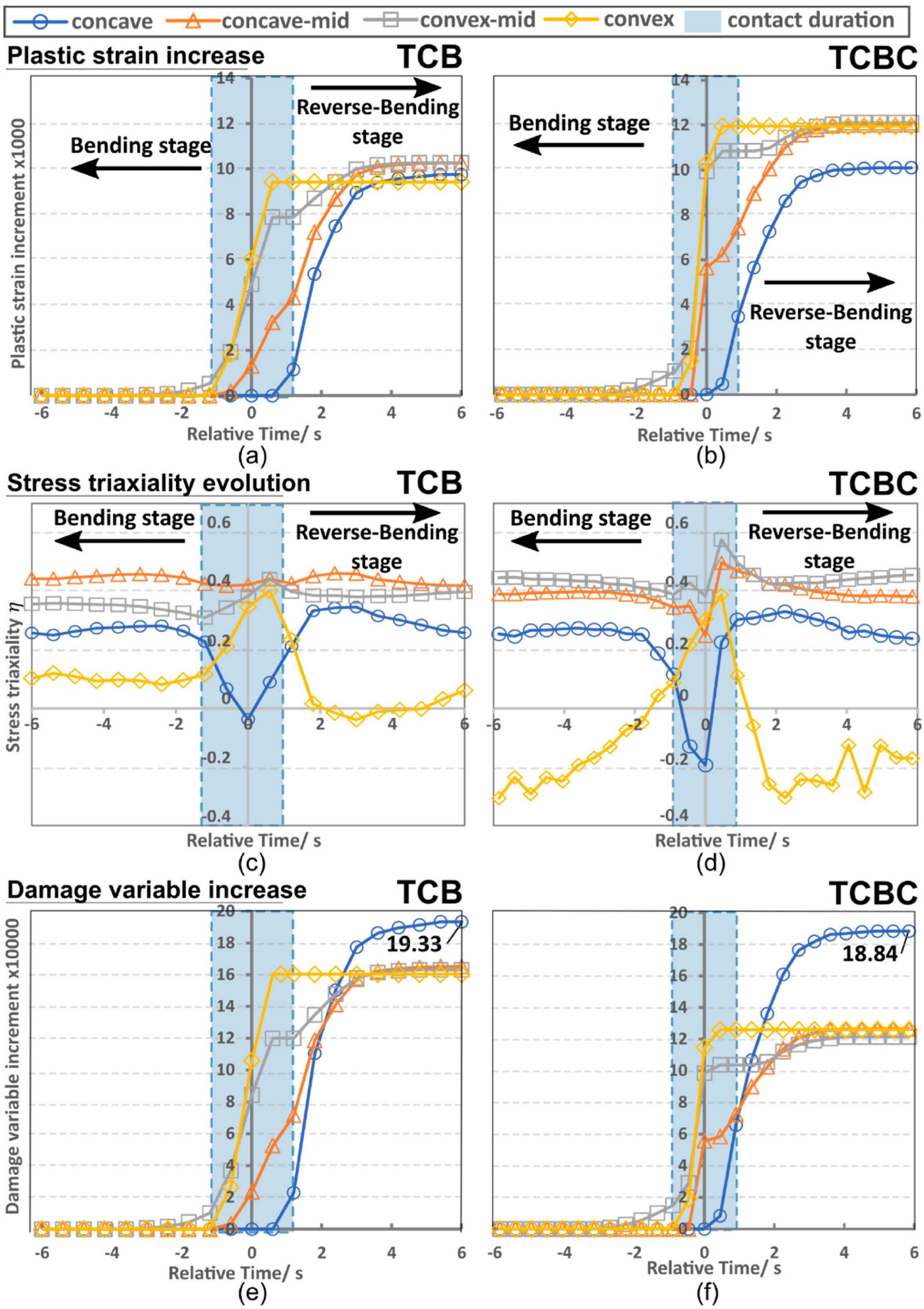

Fig. 15. Comparisons of relative equivalent strain increases, (a) and (b), stress triaxiality, (c) and (d), corresponding to damage evolution, (e) and (f), in through-thickness layers during the bending and reverse-bending strages in a single contact period of tensile under cyclic bending (TCB) and tensile under cyclic bending and compression (TCBC) processes.

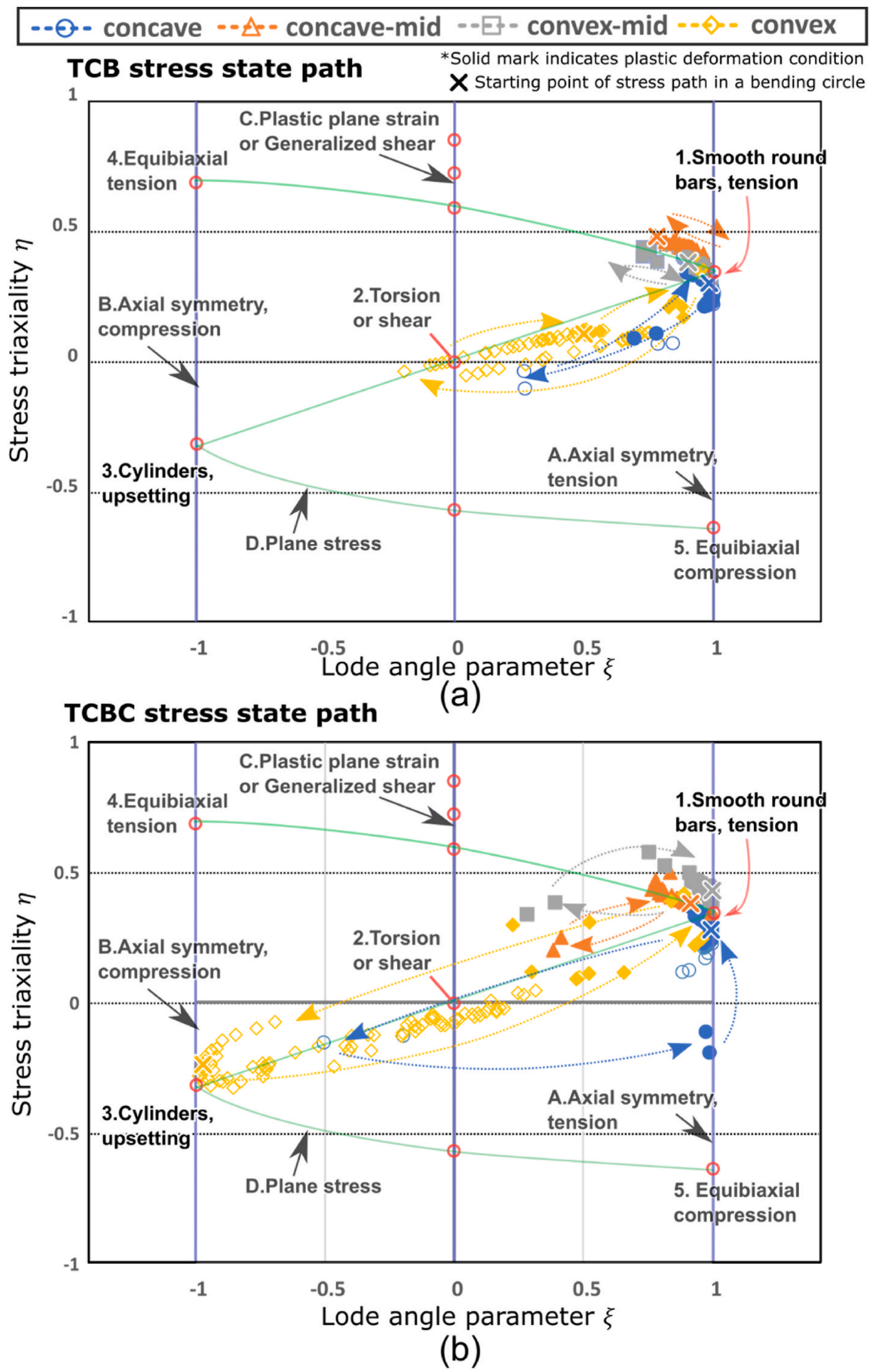

Fig. 16. Stress state path plotted on the plane of stress triaxiality and Lode angle parameter in (a) tensile under cyclic bending (TCB) and (b) tensile under cyclic bending and compression (TCBC).

a state between equi-biaxial tension and flat grooved tension.

In the DSIF process (Fig. 19b), the additional tool squeeze reduces the stress triaxiality over the entire forming stage. This leads to the increased compression and the reduced shear effect in the concave and concave-mid layers, a similar phenomenon happened in TCBC processes. The double contacts also result in the more typical equi-biaxial tension deformation on the convex side during contact, which ends at plane strain compression after the bending stage is completed.

6. Discussion

6.1. Ductile fracture in the tension under cyclic bending and the incremental sheet forming processes

The reduced damage increments due to the modification of stress state evolution in a single tool contact period was a focus of this study. Though the overall formability enhancement was known as a result of propagation by tool travelling, the stress state and damage evolutions throughout the whole deformation process can provide an overview of

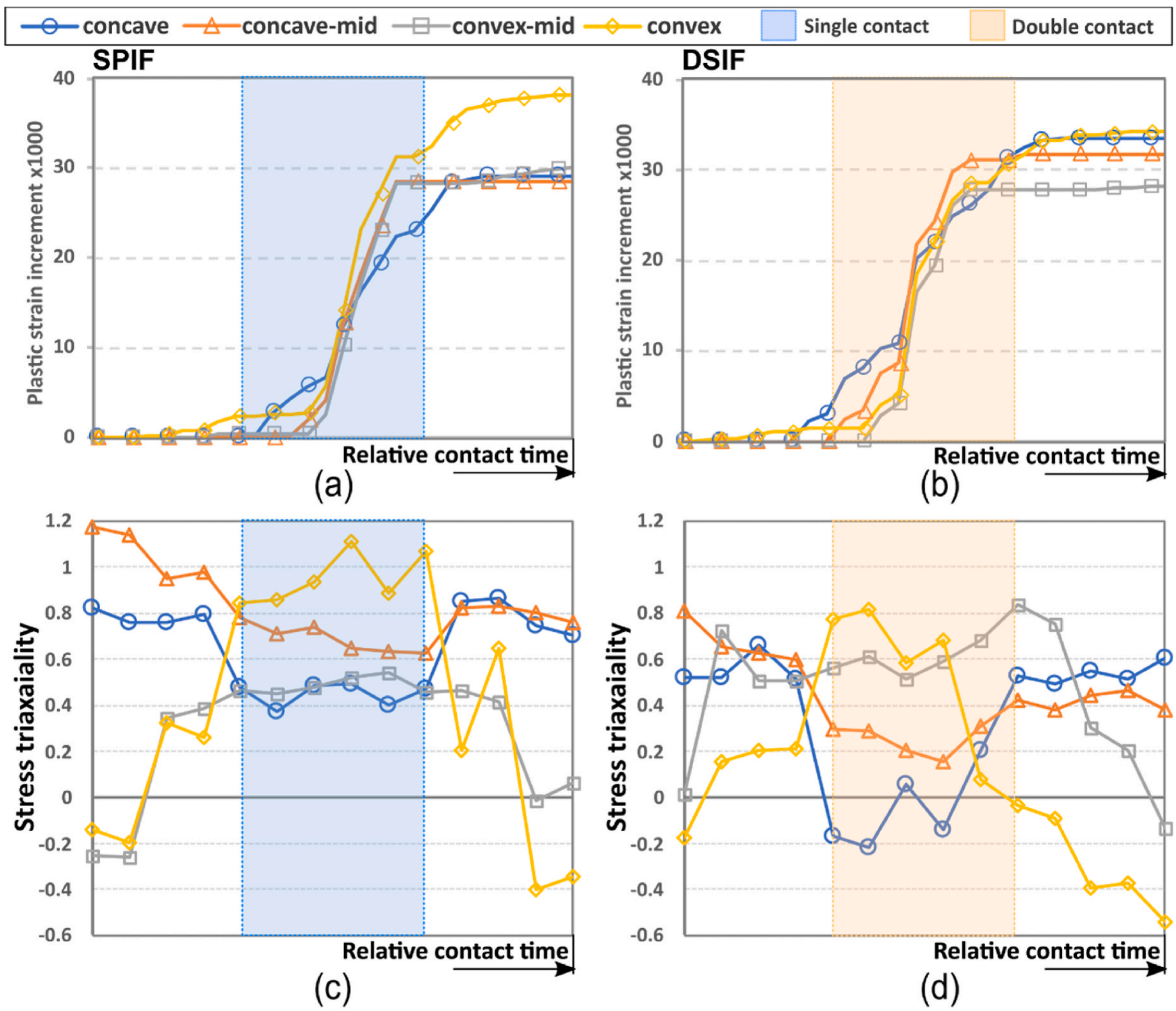

Fig. 17. Strain and stress state evolutions in a single contact cycle in section 2 of the Incremental sheet forming (ISF) processes. Relative equivalent strain increases of (a) Single point incremental forming (SPIF), and (b) Double-sided incremental sheet forming (DISF). Stress triaxiality variations by contact stages from (c) Single point incremental forming, and (d) Double-sided incremental sheet forming.

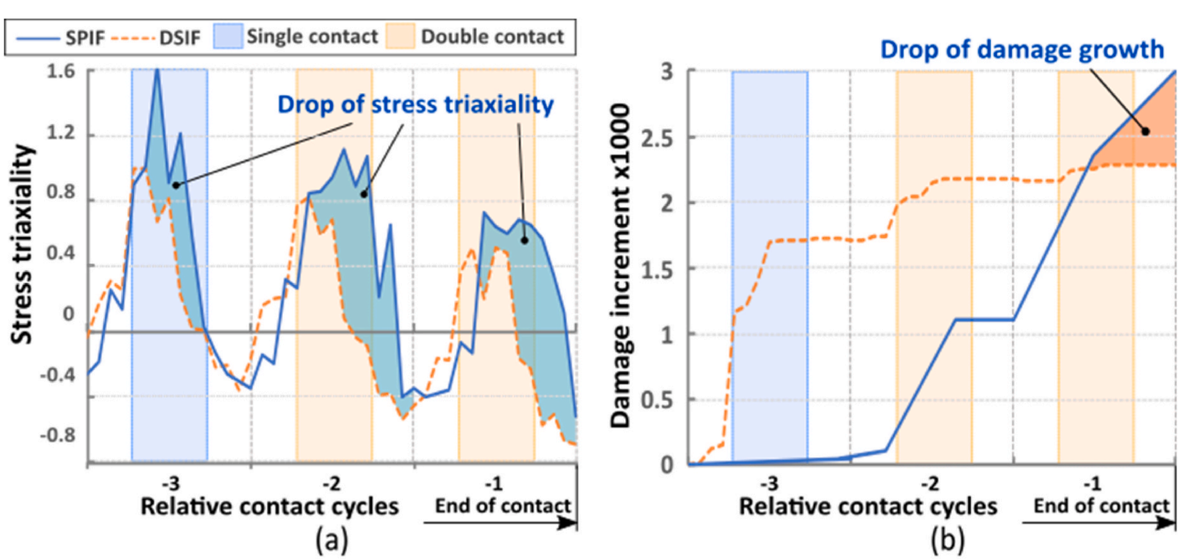

Fig. 18. Evolutions of stress triaxiality corresponding to damage under single and double contact conditions. Comparisons of (a) stress triaxiality, and (b) relative damage increases during the last 3 contact periods in section 2 of the single point incremental forming (SPIF) and double-sided incremental sheet forming (DISF) processes.

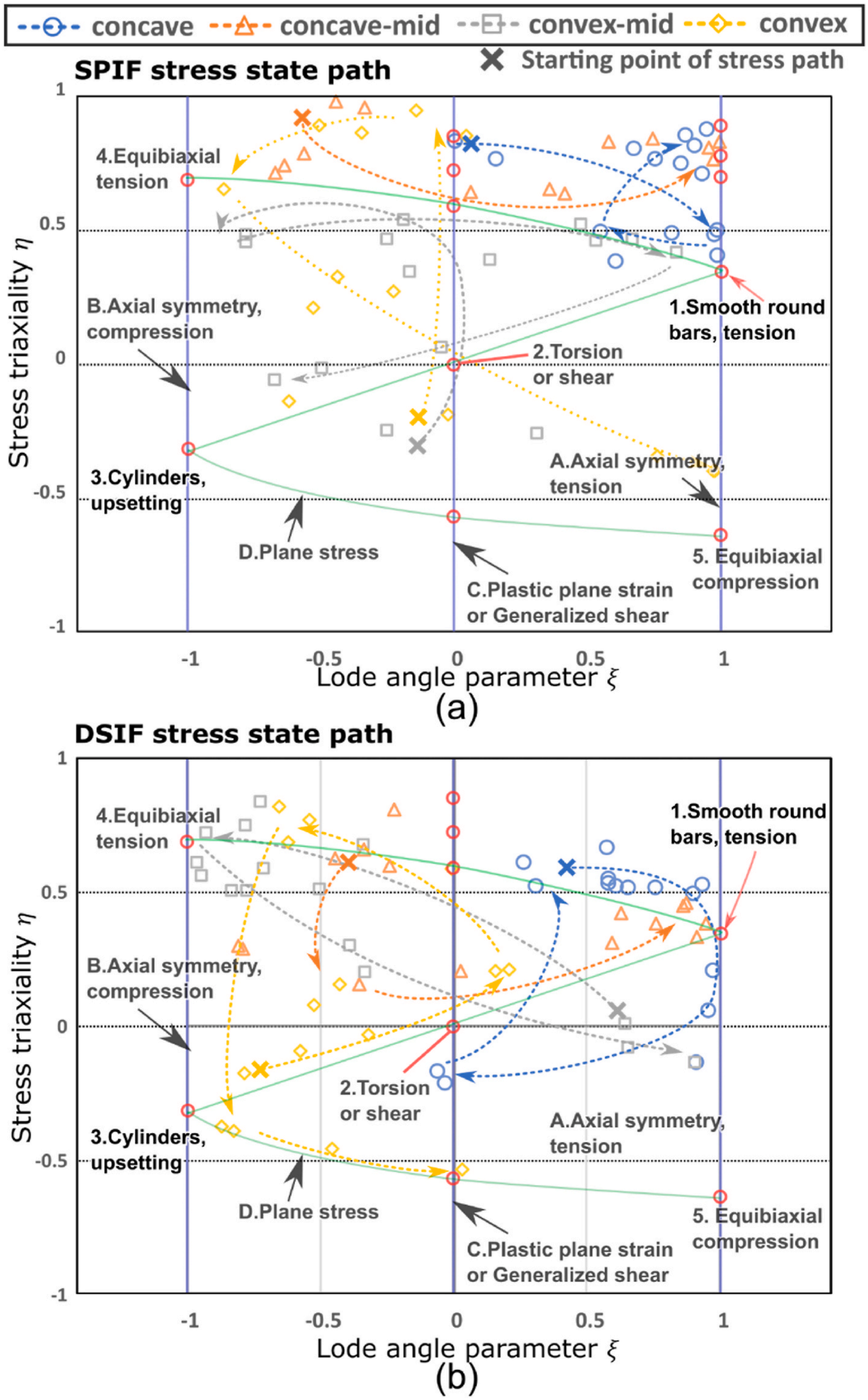

Fig. 19. Stress state path plotted on the plane of stress triaxiality and Lode angle parameter in (a) single point incremental forming (SPIF) and (b) double-sided incremental forming (DSIF).

fracture mechanisms including factors such as the continuous sheet thinning and material hardening. Fig. 20 illustrated the void volume fraction developments and the evolution of equivalent stress triaxiality and Lode angle parameter throughout the whole deformation processes in TCB, TCBC in section 2 (Fig. 12a) and the SPIF, DSIF simulations at the fracture locations. The equivalent stress triaxiality $\overline{\eta}$ and Lode angle parameter $\overline{\xi}$ are calculated using the following equations:

$$\overline{\eta} = \int \eta d\overline{\varepsilon} \Big/ \overline{\varepsilon} \tag{23}$$

$$\overline{\xi} = \int |\xi| d\overline{\varepsilon} \Big/ \overline{\varepsilon} \tag{24}$$

From Fig. 20a, the void volume fraction in the TCB for the same elongation was larger than that in the TCBC. The additional compression caused a delay of void volume fraction growth in the layers except the

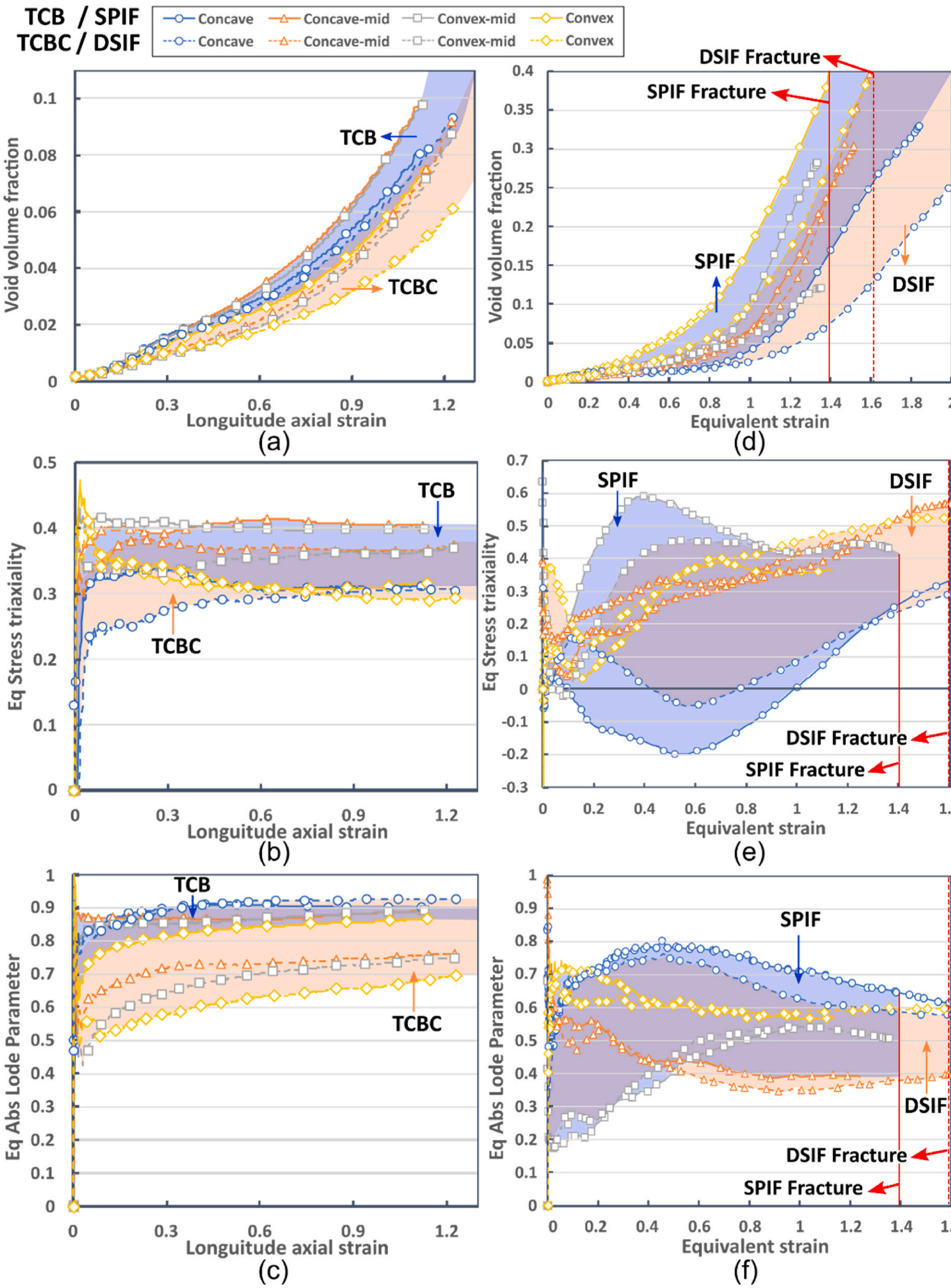

Fig. 20. Evolution of void volume fraction (a) and (d), equivalent stress triaxiality, (b) and (e), and Lode angle parameters, (c) and (f), in tensile under cyclic bending (TCB) and tensile under cyclic bending (TCBC), and in single point incremental forming (SPIF) and double-sided incremental forming (DSIF) processes. The equivalent (Eq) stress triaxiality and equivalent absolute (Eq Abs) Lode parameter are the processed parameters to indicate the tension plus compression and shear effect, respectively.

Table 3
Comparison of Gurson-Tvergaard-Needleman (GTN) models in incremental sheet forming studies.

GTN models	Guzman et al. [24]	Gatea et al. [21]	Chang and Chen [22]	New modified GTN model
Material hardening	Anisotropic plasticity hardening	Johnson-cook model	Swift flow stress model	Johnson-cook model
Shear mechanism	Nahshon and Hutchinson's modification with stress triaxiality sensitivity	Nahshon and Hutchinson's modification	Nahshon and Hutchinson's modification	Zhou's shear modification with phenomenal calibration
Coalescence mechanism	Physical-based coalescence criteria	Conventional GTN model	Oriented-coalescence criteria	Conventional GTN model
Application	1/4 SPIF conical	SPIF conical and pyramid	SPIF conical and pyramid	TCB/TCBC/SPIF/DSIF

concave layer. The gradients of void volume fraction increase on the concave layer were close in both the TCB and TCBC because the reverse-bending processes is not affected by the stress state changes in the bending stage (Fig. 20a). From the stress states point of view, the compression reduces the equivalent stress triaxiality in the TCBC (Fig. 20b), especially in the early stage of deformation. Fig. 20c shows the deformation modes tend to the uniaxial tension ($\eta \approx \frac{1}{3}, \xi = 1$) over time in both TCB and TCBC processes. The larger variation of the equivalent Lode parameter from the TCBC indicated a more significant transition from tension on the concave side to the compression on the convex side. The reason can be attributed to increased thickness reduction, leading to decreased bending ratio t/R in TCBC and less reverse-bending effect which help to improve the formability. A similar effect of wall thickness variation to the deformation mode was reported in the spinning process [48]. However, the reduced stress triaxiality was still an essential factor to the formability improvement from TCB to TCBC.

Comparing to the void volume fraction evolutions showed in Fig. 20a, d, the void volume growths in the concave layer are dissimilar between the SPIF and the DSIF processes, which indicate the reverse-bending being less significant than it in TCB and TCBC processes. Fig. 20e shows the reduced stress triaxiality variations and increased deformation stability in the DSIF over the SPIF process. It was worth noting that degeneration to the SPIF process occurred before the fracture location due to the loss of contact. However, significant differences of stress state evolutions still existed that implies the larger strain hardening and the better forming accuracy benefitting the formability of the sequential forming such as multi-pass incremental forming (MPIF). The lower values of the equivalent Lode parameter shown in Fig. 20f indicate a larger shear-induced damage in the SPIF and DSIF processes as compared to the TCB and TCBC tests, which is in agreement with previous studies [21]. It can be concluded that the bending generating tension, compression, shear and strain imbalance, followed by the pure tension in reverse-bending stage, determines the fracture in TCB, TCBC and SPIF, DSIF. Due to the less and incomplete reverse-bending cycles, also the increased stress triaxiality under biaxial tension, the ductile damage in the bending stage leads to the different fracture locations in SPIF and DSIF as compared with TCB and TCBC. The compression reduces the void growth and shear damage in double-contact region thus improves the formability in TCBC and DSIF processes.

The TCB and TCBC tests helped reveal the influences of the bending and compression and explain contradicting experimental results [12–15] of opposing effects caused by increasing a single parameter. A key question is whether the formability improved by the increase of bending and thickness can surpass the more damage generated on the convex side and the reverse-bending stage. The complex local stress states present a specific challenge to effective theoretical analysis or accurate damage prediction, which also highlights the benefit of using TCB and TCBC as a means of physical simulations of SPIF and DSIF processes.

Table 3 summarises a number of GTN models used in damage predictions in ISF studies. The previous modifications focused on the micro-scale investigation and related the maximum failure porosity to the stress state [22,24]. However, the applications were limited to SPIF processes. The disassociation with the deformation mechanism makes these modifications difficult to explain the formability improvement in DSIF process. The new GTN model modified the yield function used the experimental data and Lode function to distinguish the shear and tension-under-compression in low stress triaxiality conditions. This in-process stress-state-based modification firstly enable a correlation between the deformation modes and damage evolutions to be presented in ISF research field. However, a possible limitation is the inaccurate estimation to material hardening velocity when approaching the end of the deformation process. This includes an insufficient account to the compression effect such as the grain refinement under severe compression-tension condition similar to rolling [48], or equal channel angular extrusion (ECAE) [49], which is associated with bending as well. The effectiveness of the combined isotropic-kinematic hardening model has been confirmed in the TCB investigation [30]. There is a scope for improvement in the constitutive and damage models with the effect of material anisotropy also to be included in simulation.

6.2. Similarities and differences between the tension under cyclic bending and the incremental sheet forming processes

The incremental deformation feature and localised stress evolution through thickness, and in bending and reverse-bending stages are observed as the common characteristics in the TCB and TCBC tests, and the SPIF and DSIF processes. The comparison between the TCB and TCBC tests can capture the bending induced differences of deformation modes in the through-thickness direction, as well as the influence of changing parameters such as sheet thickness and bending depth. The TCBC tests also demonstrate the reduction of stress triaxiality and shear by the support tool postpones the damage growth during local deformation, hence improve the overall formability, the same as DSIF over SPIF. Similarly, the adverse effect on formability due to the excessive compression was reported on both TCBC and the DSIF processes [9,19]. These similar deformation characteristics offer the possibility of using TCB and TCBC processes as the indicative testing methods for SPIF and DSIF.

Even so, due to the nature of different characteristics of deformation, the results from TCB and TCBC processes cannot be directly refer to the SPIF and DSIF process. The change from 2D contact in the TCB and TCBC tests to 3D spherical contact in the SPIF and DSIF processes results in significant differences in stresses in the local deformation region. Comparing the stress paths (Figs. 16 and 19), the simplification from biaxial bending in the SPIF and DSIF ($-0.5 < \eta < 1, \xi \approx -1$) to uniaxial bending in the TCB and TCBC ($-0.3 < \eta < 0.33, \xi \approx 1$) causes the reduced stress triaxiality and asymmetric Lode angle parameter to axis $\xi = 0$. The reduced stress triaxiality highlights the dominant role of the Lode angle effect, which means the comparative results between the TCB, TCBC tests and the SPIF, DISF processes is influenced by Lode dependency of the material. From the Lode effect point of view, Nakajima tests ($\eta \approx 0.66, \xi \approx -1$) would be a closer case to the SPIF and DSIF processes. This is supported by experimental data from Gatea [43] that the fracture strains from Nakajima tests are close to SPIF test results. However, the TCB and TCBC tests provides a better flexibility for parametric studies, which is a limitation of the Nakajima test.

In conclusion, the TCB and TCBC tests provided effective validation means with intrinsic deformation mechanisms to the SPIF and DSIF processes. There are many comparable factors, such as the wall angle to the bending depth or the feed rate combined step size to the speed of oscillated roller frame movement. Therefore, the TCB and TCBC tests, in general, may be used as a way of experimental validation to the improved formability due to the effective parameter adjustments in the SPIF and DSIF processes, when the discrepancies of reverse-bending and material Lode dependency are carefully considered. They can also be implemented to investigate the effect of stress-related parameters, such as compression force and the relative tool position, the effect of different local contact conditions on formability, which is difficult to evaluate using either an analytical model or FE simulations.

7. Conclusions

This study reveals that the tension under cyclic bending (TCB), tension under cyclic bending and compression (TCBC) and single point incremental forming (SPIF), double-sided incremental forming (DSIF) processes have different deformation modes and similar mechanism of fracture. The differences of stresses and strain through thickness, generated by bending deformation, determine the occurrence of fracture. However, the identical bending mechanisms make the formability changes due to the adjustment of parameters comparable between tension under cyclic bending tests and incremental sheet forming processes. The additional compression superimposes the reduction of stress triaxiality and shear that independently improves the formability. A number of conclusions may be drawn in the following:

1) The bending induced tension, shear and compression, determined by the bending depth and thickness, and additional compression are the main factors affecting the formability change as demonstrated in the tension under cyclic bending (TCB) and tension under cyclic bending and compression (TCBC) tests. The compression reduces the stress triaxiality and shear that delays the fracture. The localised bending generates the highly localised deformation that propagated by cyclic tool movement. Hence its effect to the local stresses can affect the formability over the whole deformation process.
2) From the results presented, the new Gurson-Tvergaard-Needleman (GTN) model predicts the fracture with a better degree of accuracy, as compared to the original GTN model with Nahshon-Hutchinson's shear mechanisms. This is because the new shear mechanisms evaluate more favourably the material softening and damage accumulation due to shear for possible over-estimation of damage from a macro-scale point of view. The phenomenal calibration compensates for the coverage of shear and tension-under-compression cases, leading to the improved prediction accuracy and correlation of the damage evolution under changing deformation modes in uniaxial and biaxial bending cases.
3) The localised bending generates diverse stress states and strain discrepancy through thickness, which would be balanced in the reverse-bending stage. In the tension under cyclic bending (TCB) and tension under cyclic bending and compression (TCBC) tests, the deformation in reverse-bending stage is under pure tension and shear effect with the absence of contact pressure, which results in the increased damage accumulation as compared to the bending stage. Therefore, the ductile fracture initiates on the surface in contact with the bending roller. The fracture locations indicate the different stress states during deformation essentially determine the differences on formability.
4) For the first time, the stress paths in the plane of stress triaxiality and Lode angle parameter were used to evaluate the stress evolution of the tension under cyclic bending (TCB), tension under cyclic bending and compression (TCBC) and single point incremental forming (SPIF), double-sided incremental forming (DSIF). These stress path data provide a good insight into stress state evolution and its correlations to deformation modes in the different forming stages.
5) The single point incremental forming (SPIF) and double-sided incremental forming (DSIF) processes are essentially localised biaxial bending under tension deformation with limited forming cycles, when the tension under cyclic bending (TCB) and tension under cyclic bending and compression (TCBC) tests are mainly under plane stress deformation of axial tension. These decide the fracture started on the convex side due to the plane strain and equi-biaxial tension deformation plus the increased shear in the single point incremental forming (SPIF), double-sided incremental forming (DSIF) processes. The comparison of stress paths shows the additional compression applied by the support tool in tension under cyclic bending and compression (TCBC) and double-sided incremental forming (DSIF) plays a similar role in the formability improvement that the damage growth is benefited from the reduction of stress triaxiality and through-thickness shear in the double-sided incremental forming (DSIF) over the single point incremental forming (SPIF).

Author statement

W Peng: Conceptualization, Methodology, Validation, Investigation, Data Curation, Visualization, Writing-original draft. **H Ou:** Conceptualization, Methodology, Writing - review & editing, Supervision, Project administration.

Declaration of competing interest

The authors declare that they have no known competing financial interests or personal relationships that could have appeared to influence the work reported in this paper.

Data availability

The authors are committed to try to share relevant data in compliance with existing obligations.

Acknowledgements

The authors are grateful for Dr Shakir Gatea's kind support and suggestions in the development of the new modified GTN model; for Professor Hui Long at University of Sheffield for her permission in using their TCB and TCBC rig to conduct the TCB and TCBC tests and for Prof Jun Chen's kind support and Dr Meng Li's assistance to complete the SPIF and DSIF processes in using their DSIF machine at Shanghai Jiaotong University. The authors acknowledge the support of the Engineering and Physical Sciences Research Council [grant number EP/W010089/1].

References

[1] J.R. Duflou, A.-M. Habraken, J. Cao, R. Malhotra, M. Bambach, D. Adams, H. Vanhove, A. Mohammadi, J. Jeswiet, Single point incremental forming: state-of-the-art and prospects, International Journal of Material Forming 11 (6) (2018) 743–773, https://doi.org/10.1007/s12289-017-1387-y.
[2] K. Jackson, J. Allwood, The mechanics of incremental sheet forming, J. Mater. Process. Technol. 209 (2009) 1158–1174.
[3] R. Malhotra, L. Xue, T. Belytschko, J. Cao, Mechanics of fracture in single point incremental forming, J. Mater. Process. Technol. 212 (2012) 1573–1590.
[4] W.C. Emmens, A.H. van den Boogaard, An overview of stabilizing deformation mechanisms in incremental sheet forming, J. Mater. Process. Technol. 209 (2009) 3688–3695.
[5] M.B. Silva, M. Skjoedt, P.A.F. Martins, N. Bay, Revisiting the fundamentals of single point incremental forming by means of membrane analysis, Int. J. Mach. Tool Manufact. 48 (2008) 73–83.
[6] D. Afonso, R. Alves de Sousa, R. Torcato, Integration of design rules and process modelling within SPIF technology-a review on the industrial dissemination of single point incremental forming, Int. J. Adv. Manuf. Technol. 94 (2018) 4387–4399.

[7] A. Göttmann, J. Diettrich, G. Bergweiler, M. Bambach, G. Hirt, P. Loosen, R. Poprawe, Laser-assisted asymmetric incremental sheet forming of titanium sheet metal parts, J. Inst. Eng. Prod. 5 (2011) 263–271.
[8] H. Ren, F. Li, N. Moser, D. Leem, T. Li, K. Ehmann, J. Cao, General contact force control algorithm in double-sided incremental forming, CIRP Annals 67 (2018) 381–384.
[9] B. Lu, Y. Fang, D.K. Xu, J. Chen, S. Ai, H. Long, H. Ou, J. Cao, Investigation of material deformation mechanism in double side incremental sheet forming, Int. J. Mach. Tool Manufact. 93 (2015) 37–48.
[10] V. Kiridena, R. Verma, T. Gutowski, J. Roth, in: Rapid Freeform Sheet Metal Forming: Techology Development and Asystem Verification, U.S.D.o. Energy, 2017.
[11] W. Peng, H. Ou, A. Becker, Double-sided incremental forming: a review, J. Manuf. Sci. Eng. 141 (2019), 050802.
[12] M.B. Silva, P.S. Nielsen, N. Bay, P.A.F. Martins, Failure mechanisms in single-point incremental forming of metals, Int. J. Adv. Manuf. Technol. 56 (2011) 893–903.
[13] M. Ham, J. Jeswiet, Forming limit curves in single point incremental forming, CIRP Annals 56 (2007) 277–280.
[14] Y. Fang, B. Lu, J. Chen, D.K. Xu, H. Ou, Analytical and experimental investigations on deformation mechanism and fracture behavior in single point incremental forming, J. Mater. Process. Technol. 214 (2014) 1503–1515.
[15] Z. Liu, Y. Li, P.A. Meehan, Experimental investigation of mechanical properties, formability and force measurement for AA7075-O aluminum alloy sheets formed by incremental forming, Int. J. Precis. Eng. Manuf. 14 (2013) 1891–1899.
[16] P.A.F. Martins, N. Bay, M. Skjoedt, M.B. Silva, Theory of single point incremental forming, CIRP Annals 57 (2008) 247–252.
[17] P. Eyckens, B. Belkassem, C. Henrard, J. Gu, H. Sol, A.M. Habraken, J.R. Duflou, A. Van Bael, P. Van Houtte, Strain evolution in the single point incremental forming process: digital image correlation measurement and finite element prediction, Int. J. Material Form. 4 (2011) 55–71.
[18] N. Moser, D. Pritchet, H. Ren, K.F. Ehmann, J. Cao, An efficient and general finite element model for double-sided incremental forming, J. Manuf. Sci. Eng. 138 (2016), 091007.
[19] S. Ai, R. Dai, H. Long, Investigating formability enhancement in double side incremental forming by developing a new test method of tension under cyclic bending and compression, J. Mater. Process. Technol. 275 (2020), 116349.
[20] Z.D. Chang, M. Li, J. Chen, Analytical modeling and experimental validation of the forming force in several typical incremental sheet forming processes, Int. J. Mach. Tool Manufact. 140 (2019) 62–76.
[21] S. Gatea, H.G. Ou, B. Lu, G. McCartney, Modelling of ductile fracture in single point incremental forming using a modified GTN model, Eng. Fract. Mech. 186 (2017) 59–79.
[22] Z. Chang, J. Chen, A new void coalescence mechanism during incremental sheet forming: ductile fracture modeling and experimental validation, J. Mater. Process. Technol. 298 (2021), 117319.
[23] J. Li, S. Li, Z. Xie, W. Wang, Numerical simulation of incremental sheet forming based on GTN damage model, Int. J. Adv. Manuf. Technol. 81 (2015) 2053–2065.
[24] C.F. Guzmán, S. Yuan, L. Duchêne, E.I. Saavedra Flores, A.M. Habraken, Damage prediction in single point incremental forming using an extended Gurson model, Int. J. Solid Struct. 151 (2018) 45–56.
[25] Z. Chang, J. Chen, Analytical modeling of fracture strain and experimental validation in incremental sheet forming, J. Mater. Process. Technol. 294 (2021), 117118.
[26] W.C. Emmens, A.H. van den Boogaard, Incremental forming by continuous bending under tension—an experimental investigation, J. Mater. Process. Technol. 209 (2009) 5456–5463.
[27] W.C. Emmens, A.H. van den Boogaard, Cyclic stretch-bending: mechanics, stability and formability, J. Mater. Process. Technol. 211 (2011) 1965–1981.
[28] T.J. Roemer, T.J. Barrett, M. Knezevic, B.L. Kinsey, Y.P. Korkolis, Experimental study of continuous-bending-under-tension of AA6022-T4, J. Mater. Process. Technol. 266 (2019) 707–714.
[29] M. Knezevic, C.M. Poulin, X. Zheng, S. Zheng, I.J. Beyerlein, Strengthening of alloy AA6022-T4 by continuous bending under tension, Mater. Sci. Eng. 758 (2019) 47–55.
[30] T.J. Barrett, S. Takagi, N. Islam, T. Kuwabara, T. Hassan, B.L. Kinsey, M. Knezevic, Y.P. Korkolis, Material modeling and simulation of continuous-bending-under-tension of AA6022-T4, J. Mater. Process. Technol. (2020), 116658.
[31] J.C. Benedyk, B.L. Kinsey, Y.P. Korkolis, T.J. Roemer, Fundamental studies of continuous bending under tension (CBT) and potential automotive forming applications, Mater. Today Proc. 2 (2015) 4998–5005.
[32] J.M. Allwood, D.R. Shouler, A.E. Tekkaya, The increased forming limits of incremental sheet forming processes, Key Eng. Mater. 344 (2007) 621–628.
[33] Y. Bai, T. Wierzbicki, A comparative study of three groups of ductile fracture loci in the 3D space, Eng. Fract. Mech. 135 (2015) 147–167.
[34] Y. Bai, T. Wierzbicki, A new model of metal plasticity and fracture with pressure and Lode dependence, Int. J. Plast. 24 (2008) 1071–1096.
[35] J. Zhou, X. Gao, J.C. Sobotka, B.A. Webler, B.V. Cockeram, On the extension of the Gurson-type porous plasticity models for prediction of ductile fracture under shear-dominated conditions, Int. J. Solid Struct. 51 (2014) 3273–3291.
[36] K. Nahshon, J.W. Hutchinson, Modification of the Gurson model for shear failure, Eur. J. Mech. Solid. 27 (2008) 1–17.
[37] S. Gatea, D. Xu, H. Ou, G. McCartney, Evaluation of formability and fracture of pure titanium in incremental sheet forming, Int. J. Adv. Manuf. Technol. 95 (2017) 625–641.
[38] V. Tvergaard, A. Needleman, D.T.H. Dcamm, Analysis of the Cup-Cone Fracture in a Round Tensile Bar, Technical University of Denmark, 1983.
[39] A.L. Gurson, Continuum theory of ductile rupture by void nucleation and growth: Part I—yield criteria and flow rules for porous ductile media, J. Eng. Mater. Technol. 99 (1977) 2–15.
[40] L. Xue, Constitutive modeling of void shearing effect in ductile fracture of porous materials, Eng. Fract. Mech. 75 (2008) 3343–3366.
[41] L. Malcher, F.M. Andrade Pires, J.M.A. César de Sá, An extended GTN model for ductile fracture under high and low stress triaxiality, Int. J. Plast. 54 (2014) 193–228.
[42] H. Wu, W. Xu, D. Shan, B.C. Jin, An extended GTN model for low stress triaxiality and application in spinning forming, J. Mater. Process. Technol. 263 (2019) 112–128.
[43] S. Gatea, Experimental and numerical investigation of formability and ductile fracture in incremental sheet forming, in: Faculty of Engineering, University of Nottingham, Nottingham, UK, 2017.
[44] J. Zhai, T. Luo, X. Gao, S.M. Graham, M. Baral, Y.P. Korkolis, E. Knudsen, Modeling the ductile damage process in commercially pure titanium, Int. J. Solid Struct. 91 (2016) 26–45.
[45] L.E. Dæhli, D. Morin, T. Børvik, O.S. Hopperstad, A Lode-dependent Gurson model motivated by unit cell analyses, Eng. Fract. Mech. 190 (2018) 299–318.
[46] Z.G. Liu, W.H. Wong, T.F. Guo, Void behaviors from low to high triaxialities: transition from void collapse to void coalescence, Int. J. Plast. 84 (2016) 183–202.
[47] W. Peng, Experimental and numerical investigations of deformation and fracture mechanisms in double-sided incremental forming, in: Faculty of Engineering, University of Nottingham, Nottingham, UK, 2022.
[48] P.F. Gao, X.G. Yan, F.G. Li, M. Zhan, F. Ma, M.W. Fu, Deformation mode and wall thickness variation in conventional spinning of metal sheets, Int. J. Mach. Tool Manufact. 173 (2022), 103846.
[49] Y.W. Tham, M.W. Fu, H.H. Hng, Q.X. Pei, K.B. Lim, Microstructure and properties of Al-6061 alloy by equal channel angular extrusion for 16 passes, Mater. Manuf. Process. 22 (2007) 819–824.